Ice Cloud Particle Size Distributions and Pressure-Dependent Terminal Velocities from In Situ Observations at Temperatures from 0° to −86°C

ANDREW J. HEYMSFIELD, CARL SCHMITT, AND AARON BANSEMER

NCAR, Boulder, Colorado

(Manuscript received 24 April 2012, in final form 5 March 2013)

ABSTRACT

The primary goal of this study is to derive ice particle terminal velocities from micron to centimeter sizes and for atmospheric pressures covering the range 200–1000 hPa from data spanning a wide range of locations, temperatures, and altitudes and to parameterize the results for use in cloud through cloud models. The study uses data from 10 field programs spanning the temperature range −86° to 0°C and encompassing a total of about 800 000 km of cloud horizontal pathlengths and includes measurements of ice particle size distributions (PSDs) and direct measurements of the ice water content (IWC). The necessary ice particle variables are derived using variables that are interconnected rather than varying independently from observations reported in the literature. A secondary goal of the study is to quantify the properties of ice cloud particle ensembles over a wide range of temperatures to further the understanding of how ice particle ensembles and ice clouds develop.

Functional forms for the PSDs and mass– and area–dimensional relationships are developed from the observations and summarized in a table. The PSDs are found to be nearly exponential at temperatures from about −40° to −10°C although deviations from exponentiality are noted outside of this range. It is demonstrated that previous pressure-dependent corrections to ice fall speeds lead to overestimated terminal velocities for particles smaller than 1 mm, particularly so for sizes below 100 μm, with consequent effects on modeled lifetimes of cold ice clouds.

1. Introduction

Ice clouds are an important modulator of Earth's climate system given their global coverage—more than 33% (Wylie et al. 2005)—and the range of heights (from 0 to >18 km) and temperatures T (from −90° to 3°C) that they occupy. Ice clouds contribute significantly to Earth's radiation budget through combined effects on solar shortwave reflection and longwave trapping (e.g., Hartmann and Short 1980). Ice clouds also play a significant role in Earth's hydrologic cycle as a result of both precipitation generation and their effect on the thermal structure of the troposphere and associated cloud dynamics. Accurate characterization of their effects on Earth's climate system and hydrological cycles requires general circulation models (GCMs); large disagreements in the representation of ice clouds among these models (Li et al. 2005, 2007), however, have led to wide variations in the quantitative descriptions of such effects (Intergovernmental Panel on Climate Change Fourth Assessment Report). This disparity demonstrates the importance of addressing GCM deficiencies if we are to model the climate system and hydrologic cycle in a changing world.

Because accurate estimation of the ice water content (IWC) distribution globally is a central parameter for evaluating and improving climate model predictions of current and future climate (Stephens et al. 2002), it is especially important to obtain accurate estimates of the IWC throughout the range of temperatures, altitudes, and latitudes found in the troposphere.

In addition, ice particle sedimentation velocities influence global ice cloud coverage and longevity and, indirectly, their radiative properties (Sanderson et al. 2008). Velocities for ensembles of ice cloud particles as a function of temperature, altitude (pressure), and cloud formation mechanism are related to the ice particle size distributions (PSDs) and corresponding particle masses and cross-sectional areas (Heymsfield and Westbrook 2010).

Interpreting ice cloud properties from global measurements with active or passive satellite measurements

Corresponding author address: Andrew Heymsfield, NCAR, 3450 Mitchell Lane, Boulder, CO 80301.
E-mail: heyms1@ucar.edu

DOI: 10.1175/JAS-D-12-0124.1

TABLE 1. Summary of field program datasets.

Project	No. of flights	Cloud formation designation	Lat, lon	In-cloud temperatures (°C)	No. of 5-s PSDs
ARM2000	7	Stratiform	37°, −98°	−52° to 0°	6637
CF	11	Convective	25°, −82°	−63° to 0°	13 052
TC4	11	Convective	16°, −84°	−57° to 0°	17 715
NAMMA	12	Convective	16°, −24°	−54° to 0°	15 913
AIRS	9	Stratiform	44°, −79°	−47° to 0°	9573
C3VP	4	Stratiform	46°, −74°	−42° to −1°	6471
REPLICATOR	3	Stratiform	37°, −96°	−63° to −40°	31
SCOUT	5	Stratiform	13°, −85°	−87° to −65°	3379
SUBVIS	3	Stratiform	30°, −95° 16°, −84° −12°, 131°	−83° to −57°	455
MPACE	13	Stratiform	71°, −157°	−57° to 0°	9579

requires accurate estimates of all or some of the following information: PSDs and crystal habits (shapes) and crystal surface structure as a function of temperature, and whether cloud formation is via convection or in situ generation, among others. Determination of the IWC and precipitation rates can potentially be improved through a self-consistent set of retrieval algorithms.

A number of researchers have presented in-depth analyses of in situ measurements of PSDs and derived analytic representations for them (e.g., Houze et al. 1979; Heymsfield and Platt 1984; McFarquhar and Heymsfield 1997; Heymsfield et al. 2002; Delanoë et al. 2005; Field et al. 2005, 2007; Tian et al. 2010). A primary objective of these studies has been to find a few parameters that are sufficient to describe the entire PSD. Some of these authors have developed normalized PSDs using one or two moments of the PSD and some have included multiple representations that account for different parts of the PSDs. This study seeks to improve upon earlier studies as it has become increasingly accepted from measurements in wind tunnels and with improved instrumentation that ice particle observations reported in many of these earlier were compromised because of shattering of ice particles on the inlets of those instruments designed to measure them (Korolev et al. 2011). The most up-to-date artifact removal techniques have been used in our study to try to minimize contributions due to shattered particles as much as possible yet still include a wide range of temperatures and geographical locations.

The present study reports on ice PSDs and their bulk properties—such as ice water content and terminal velocities—as part of a continuing effort to improve the parameterizations of these properties in cloud, weather forecasts, and climate models. The first objective of this study is to develop a geographically diverse set of relationships between the PSDs and temperature, with particular emphasis on temperatures below −50°C where data are sparse. The field program datasets used for this study include direct measurements of the condensed water content with one exception, from our balloon-borne ice crystal replicators. This allows us to estimate ice particle masses and fall speeds more accurately than without those direct measurements. Functional fits to the PSDs, mass–dimensional relationships, and area–diameter relationships are derived according to whether the clouds are generated via deep convection or in situ production. These observations lay the groundwork for further refinement of the algorithms used to retrieve ice cloud properties from active and passive spaceborne sensors.

2. Data

Tables 1 and 2 summarize the datasets and probes used. The particles observed in ice clouds and their size distribution provide valuable information regarding the dependence of the PSD properties on temperature and the bulk properties of ice clouds. Particle size D is the approximate maximum diameter $D_{\max}$ of a particle; $D_{\max}$ is the smallest diameter of a circle that fully encloses the projected 2D image of a particle as imaged by particle probes or by impactors. The probes generally give images of particles in their approximate fall orientation.

The ice cloud data used for this study include geographical locations from the Arctic to the tropics, span a temperature range from −86° to 0°C, and cover an altitude range from near the surface to 19 km (Fig. 1 and Table 1). Data for temperatures between −60° and −86°C (section 2a) come from the upper parts of low- and mid-latitude clouds, where few in situ observations have been reported. At these temperatures, sub-200-μm-diameter particles dominate the observations. Data for temperatures warmer than −60°C (section 2b) come from a combination of in situ–generated cirrus in the Arctic

TABLE 2. Microphysical particle probes. A value of 0 means available, but not used.

Project	FSSP	CAS	VIPS	Rep	2DC	CIP	2DP	PIP	HVPS	Condensed water content	RICE
ARM2000	0				X		X			CVI	X
CF	0				X				X	CVI	X
TC4		X				X		X		CVI	X
NAMMA		X				X		X		CVI	
AIRS	0				X		X			CSI	X
C3VP	0				X		X			CSI	X
REPL.				X						N/A	
SCOUT	X					X				FISH/FLASH	X
SUBVIS			X		X					CLH/Harvard	X
MPACE	0				X		N/A			CSI	X

and midlatitudes and convectively generated cirrus clouds at low latitudes. These data, mostly taken at 1 Hz, are averaged over 5-s intervals corresponding to approximately 1-km horizontal pathlengths (except for the balloonborne Replicator observations discussed later). A fixed duration or pathlength is desirable to improve the statistics over 1-Hz sampling intervals; averaging over variable pathlengths would introduce further meteorological uncertainties by averaging features such as generating cells and convective turrets in different ways. Furthermore, a 1-km pathlength is desirable because it corresponds very roughly to what

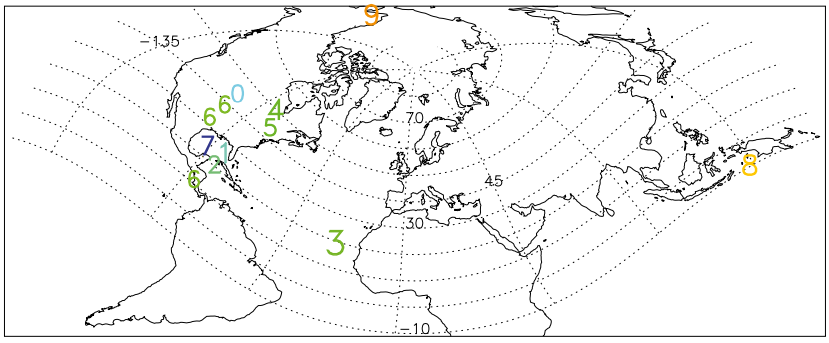

0–ARM: ARM 2000, Atmospheric Radiation Measurement (ARM) Field Campaign, 2000
1: CF: CRYSTAL–FACE, The Cirrus Regional Study of Tropical Anvils and Cirrus Layers – Florida Area Cirrus Experiment, 2002
2: TC4: The Tropical Composition, Cloud and Climate Coupling (TC4) Field Campaign, 2007
3: NAM: NAMMA – The NASA African Monsoon Multidisciplinary Analyses Campaign, 2006
4: AIRS: AIRS_2, Alliance Icing Research Study II, 2003–2004
5: C3VP: Canadian CloudSat/CALIPSO Validation Program, 2006–2007
6: Rep: Replicator Observations, First ISCCP Research Experiment (FIRE)–2, 1991
7: SV, Subvisual: Experiments with CF and pre–AURA Validation Experiment, 2002 and 2004
8: SCT, SCOUT: StratosphericDClimate Links w/Emphasis on the Upper Troposphere/Lower Stratosphere, 2003
9: MPACE: Mixed–Phase Arctic Cloud Experiment, 2004

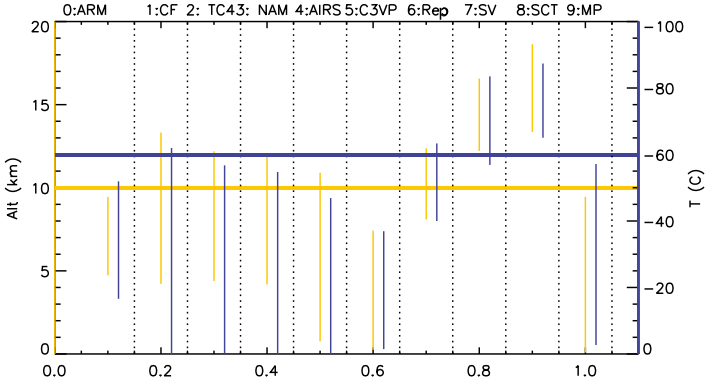

FIG. 1. Field projects and summary of observations. (top) Geographic locations, with field program acronym defined. (bottom) Altitude ranges (left ordinate) and temperature ranges (right ordinate) defined. Colors distinguish the different field programs.

radar would sample in the horizontal from the ground or space. A Bayesian approach to upscaling our 1-km PSDs to a pathlength more relevant to climate modeling is developed in Jameson and Heymsfield (2013). They use correlation statistics with a set of particle size distribution measurements acquired during a 79-km horizontal leg through a continuous ice cloud during the Tropical Clouds, Convection, Chemistry and Climate field program (TC4) discussed later in order to provide a physically based approach to the problems of upscaling and downscaling of particle size distributions and their integrable properties without arbitrary assumptions. The effects of shattering of ice particles on the leading surfaces of the probes designed to measure them (Gardiner and Hallett 1985; Korolev and Isaac 2005; Field et al. 2006; Heymsfield et al. 2008; Korolev et al. 2011) are discussed and evaluated when necessary.

a. Observations of colder ice clouds

1) CRYSTAL-FACE (WB57) AND PREAVE

Data collected at low temperatures from two flights by the National Aeronautics and Space Administration (NASA) WB57 during the Cirrus Regional Study of Tropical Anvils and Cirrus Layers–Florida-Area Cirrus Experiment [CRYSTAL-FACE (CF, and, where necessary, CF-Low Temperature)] and from one flight between Houston and Costa Rica during the Pre-*Aura* Validation Experiment (PreAVE) are used in our study (Fig. 1, No. 7). An overview of the results from those two programs [referred to as subvisual (SV)] is presented in Schmitt and Heymsfield (2009).

The CF data were collected in high-altitude, nonconvective thin clouds with temperatures from about −60° to −86°C (Table 1; Fig. 1, bottom, and Fig. 2a). One case comprises data when the NASA WB57 repeatedly sampled anvil cirrus in varying stages of development. Initial passes through the cloud field intercepted decaying anvil cloud from convection occurring on previous days. Later in the flight, more recently generated anvil clouds were intercepted. During a second CF flight, the WB57 sampled tropopause cirrus near the Honduran coast. Satellite data showed gravity waves containing cirrus that radiated away from the Honduran convection. During the PreAVE flight, the WB57 intercepted a tropopause cirrus layer.

Ice water content was measured by the University of Colorado closed-path tunable diode laser hygrometer (CLH) for CF and the Harvard University Lyman-Alpha total water photofragment–fluorescence hygrometer for PreAVE (Davis et al. 2007) (Table 1). The detection threshold of these instruments is about $10^{-4}\,\mathrm{g\,m^{-3}}$, and the precision is about $10^{-4}\,\mathrm{g\,m^{-3}}$. We have used data when this detection limit and precision were met.

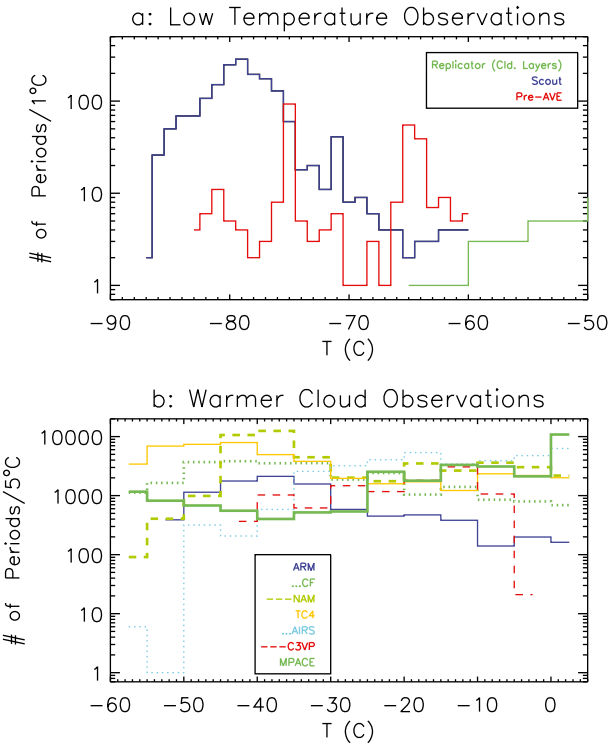

FIG. 2. Distribution of number of periods with measured PSDs (5-s averages) as a function of temperature for (a) $T < -60$°C and (b) $T > -60$°C. The field programs are identified by color.

Particle size distributions on the WB57 were measured with the National Center for Atmospheric Research (NCAR) video ice particle sampler (VIPS) probe, which provides shape and concentration information for particles with sizes from 10 to 350 μm—a poorly understood size range. The usable sample volume of the VIPS is approximately $0.84\,\mathrm{L\,s^{-1}}$ at an airspeed of $160\,\mathrm{m\,s^{-1}}$ and for particles above 10-μm diameter, or about a factor of 9 larger than the 2DC and 2DS probes for 50-μm particles and a factor of 3 larger than for a 20-μm particle imaged by the 2DS probe. For a 20-μm particle imaged by the 2DS and VIPS probes, the VIPS has about a 9-times-larger sample volume. Ice crystals impact a transparent moving belt and then are imaged and recorded by a video microscope. The images are analyzed with software to determine size and shape properties. Derived properties for each particle from VIPS include their projected area and maximum dimension, which are binned into size distributions. Shattering on the small particle and imaging probes produces small ice crystals; this process does not affect the VIPS because there are few larger particles and it is easy to identify shattered elements if present. Data from a 2DC probe were used for particles above 200 μm.

2) FIRE-II (REPLICATOR)

During the First International Satellite Cloud Climatology Project (ISCCP) Regional Experiment, phase II (FIRE-II) field campaign based out of Coffeyville, Kansas, in November and December 1991, in situ–generated cirrus clouds were targeted (Table 1 and Fig. 1, No. 6). Balloonborne ice crystal Replicators provided vertical profiles of the PSD and detailed ice crystal habit information and cross-sectional areas for particles 10 μm and above and with 1.4-μm resolution (Miloshevich and Heymsfield 1997). Particle shattering is again insignificant, owing to the roughly 4 m s^{-1} ascent velocity of the balloons, and collection efficiency for small particles was measured in a wind tunnel. The Replicators have a sample volume of about 6 L s^{-1} or about 200 times larger for 25-μm particles than the 2DC imaging probe. In addition, the more desirable quasi-vertical profiles rather than horizontal legs or spiral descents were obtained through the cloud layer. Temperature and pressure were recorded through the ascents. The IWCs were derived using the Schmitt and Heymsfield (2009) mass–dimensional relationships.

Replicator data are from three ascents through cloud bottom to top and focus on the temperature range −63° to −50°C (Fig. 1, bottom, and Fig. 2a). Derived properties for each particle include their projected area and diameter. Averaged PSDs are derived by dividing the cloud layer into 15 equal height layers; these layers range from 170 to 270 m deep, depending on the case. This vertical resolution is intermediate between *Cloud–Aerosol Lidar and Infrared Pathfinder Satellite Observations* (*CALIPSO*) and *CloudSat* vertical resolution for the altitudes sampled.

3) SCOUT

We reanalyzed data reported in the de Reus et al. (2009) study of cold cloud measurements from the Stratospheric–Climate Links with Emphasis on the Upper Troposphere and Lower Stratosphere (SCOUT) field program based out of Darwin, Northern Territory, Australia, in November–December 2005 (Vaughan et al. 2008; see Fig. 1, No. 8) . These data were collected from one survey flight and four flights during the period 25–30 November 2005, in the vicinity of ''Hector storms'' (intense deep thunderstorms), but were usually well removed from them. The predominance of SCOUT samples used in this analysis was in the temperature range −75° to −85°C (Fig. 1, bottom, and Fig. 2a).

The PSDs were measured by a Particle Measuring Systems (PMS) Forward Scattering Spectrometer Probe (FSSP-100) that used Droplet Measurement Technologies (DMT) high-speed electronics (SPP-100), with concentrations derived for seven size bins centered in sizes from 4 to 28 μm, and by a DMT Cloud Imaging Probe (CIP), with concentrations derived in 19 size bins from 50 μm to greater than 1 mm. The PSDs are obtained in 1-s intervals using the processing techniques discussed in de Reus et al. (2009); these PSDs are averaged in 5-s intervals, or 750 m to 1 km of pathlength at a true airspeed of 150 or 200 m s^{-1}, to improve their statistical significance.

The FSSP and 2DC or CIP concentration data have notable limitations: the sample volume of the FSSP is relatively small, requiring concentrations of order 3 L^{-1} (over a 5-s average at typical research aircraft flight speeds) in any one size bin to detect a single particle; the FSSP sizing is calibrated using spheres, with the result that nonspherical particles (e.g., columns with length/width dimensions greater than 2 or 3) are undersized, and the 2DC/CIP probes undersize particles and underestimates the nominal (manufacturer provided) sample volume in particle sizes below 100–200 μm, but quantitative evaluations of these effects on the derived concentration are difficult to estimate (Strapp et al. 2001). A detailed discussion of the sizing of the SCOUT FSSP particles is presented in the appendix.

Shattering issues are minimized by restricting the data presented to those periods where the largest 2DC particles are 200 μm or smaller, although this cutoff size is arbitrarily chosen. Jensen et al. (2009) note a strong correlation between the concentrations of small crystals [from the small particle probes—in that case a Cloud and Aerosol Spectrometer (CAS)] and the IWC in large particles (from the 2D probes—in that case a CIP). That correlation breaks down when the particles are all less than 200 μm. In regions absent of large crystals, they noted relatively few crystals detected by the CAS. The cut size of 200 μm is therefore entirely reasonable given that very low IWCs are present. Given that the focus of the SCOUT analysis is where the temperature is −70°C and below, small particles predominate. Of the PSDs measured in cloud in the SCOUT temperature range of interest, 0.2% had particles exceeding 200 μm.

Condensed water content and water vapor content were measured with two probes, measuring total water content [Fast In Situ Hygrometer (FISH); laboratory-derived accuracy of 6%] and Fluorescent Airborne Stratospheric Hygrometer (FLASH water vapor content; laboratory-derived accuracy of 8%), respectively (Schiller et al. 2008). The difference between the two measurements yielded the IWC. The total uncertainty in the derivation of the IWC from the two hygrometer instruments is estimated to be about 20% (Schiller et al. 2008).

b. Observations of warmer ice clouds

Observations from ice clouds where $T > -60°C$ include data from seven field campaigns [see Heymsfield et al. (2009, hereafter H09) and Heymsfield et al. (2010, hereafter H10), for details on six of them] and an additional field program in the Arctic (Table 1, Figs. 1 and 2b). These include the Atmospheric Radiation Measurement Program [ARM 2000 intensive observing period (IOP); 3 cold cirrus cloud flights in synoptically generated ice clouds, Oklahoma]; Cirrus Regional Study of Tropical Anvils and Cirrus Layers–Florida-Area Cirrus Experiment (CF; largely convectively generated ice clouds sampled by the University of North Dakota Citation, 10 flights); the NASA African Monsoon Multidisciplinary Analyses (NAMMA; 12 mostly convectively generated clouds, many of which formed in or near dust layers); Tropical Clouds, Convection, Chemistry and Climate (TC4; 11 flights, Costa Rica, mostly convectively generated; Toon et al. 2010); synoptically generated ice cloud layers with embedded convection and supercooled liquid water from the Alliance Icing Research Study II (AIRS-2; 7 flights, Toronto, Ontario, Canada, area; Isaac et al. 2005); and the *CloudSat*/*CALIPSO* Validation Project (C3VP; 3 flights, Montreal, Quebec, Canada, area). The Arctic field project was the Mixed-Phase Arctic Cloud Experiment (MPACE; Prudhoe Bay, Alaska, 13 flights). Air temperatures for all field programs were measured with Rosemount temperature probes.

The ARM and MPACE ice clouds have top temperatures generally less than −25°C, and those from AIRS and C3VP mostly have top temperatures greater than −25°C. The CF, NAMMA, and TC4 subfreezing periods have low cloud-top temperatures, and many of the NAMMA periods are adjacent to or within deep convection (although with liquid water periods removed; see below).

A cloud formation designation has been assigned to each field program based on the general characteristics of the clouds sampled (Table 1). Clouds sampled for CF, NAMMA, and TC4 are designated as "convective." For the other field programs, the designation is "stratiform." Although the SCOUT and some of the PA cases could be classified as convective, the sampling was conducted far enough from the convection or convective source that the large particles generated in the updrafts would have mostly fallen out upwind of the sampling.

Probe details (Table 2) are given in H09. The PSDs were acquired with a 2DC or similar Droplet Measurement Technologies (DMT) CIP probe (sizing from about 50 to 1000 μm) and a 2DP, DMT precipitation imaging probe (PIP), or high-volume precipitation spectrometer (from 200 μm to greater than 1 cm). Data from a 2DS probe (from 10 μm to greater than 1 mm; Lawson et al. 2006) during TC4 were also examined. Total condensed water content (TWC)—ice plus liquid when present—was measured with a counterflow virtual impactor (CVI) or a cloud spectrometer and impactor (CSI) for TWC > 0.01 g m^{-3}. Because of the ice shattering issue, the FSSP or CAS data are not used for small particles (see appendix A). For each PSD, the 2D (2D-C, CIP, 2D) probe data are processed to account for ice shattering using particle interarrival times (Field et al. 2006).

Liquid water presence (when $T > -40°C$) and its content was estimated from a Rosemount icing probe (RICE). Liquid water was also detected with a King probe. Neither RICE nor King probe data are available for NAMMA. We removed periods from NAMMA when CAS concentrations were above 30 cm^{-3} at temperatures above −40°C, although this cautious approach may have inadvertently removed real, small particles. Liquid water encounters identified from RICE and the King probes were infrequent and have been filtered out of the dataset.

c. Ice water content calculation from PSDs

The IWC is given by the distribution of ice mass m with D:

$$\mathrm{IWC} = \sum_{D_{\min}}^{D_{\max}} N(D)m(D), \tag{1}$$

where $D_{\min}$ and $D_{\max}$ are the minimum and maximum D of the PSD and N is the concentration of particles in size bin D. For the calculations of m in the cold-temperature cases, we use a modified version (discussed below) of the PreAVE relationship developed by Schmitt and Heymsfield (2009) based on a comparison of the PSDs with different $m(D)$ relationships with the measured IWCs:

$$m = 0.91(\pi/6)D^3 e^{-94D}, \tag{2}$$

where m is in grams and D is in centimeters. Most other studies have used power-law-type $m(D)$ relationships to derive the IWC (e.g., Brown and Francis 1995):

$$m = aD^b, \tag{3}$$

where m is again in grams, a is the coefficient (in cgs units), and b is the exponent; a power-law fit to (2) for sizes 200 μm and below yields a(cgs) = 0.0175 and b = 2.51.

The IWCs are calculated from the PSDs using three sets of power-law coefficients. We refer to these as "sets" for brevity. Set 1 uses the standard power-law

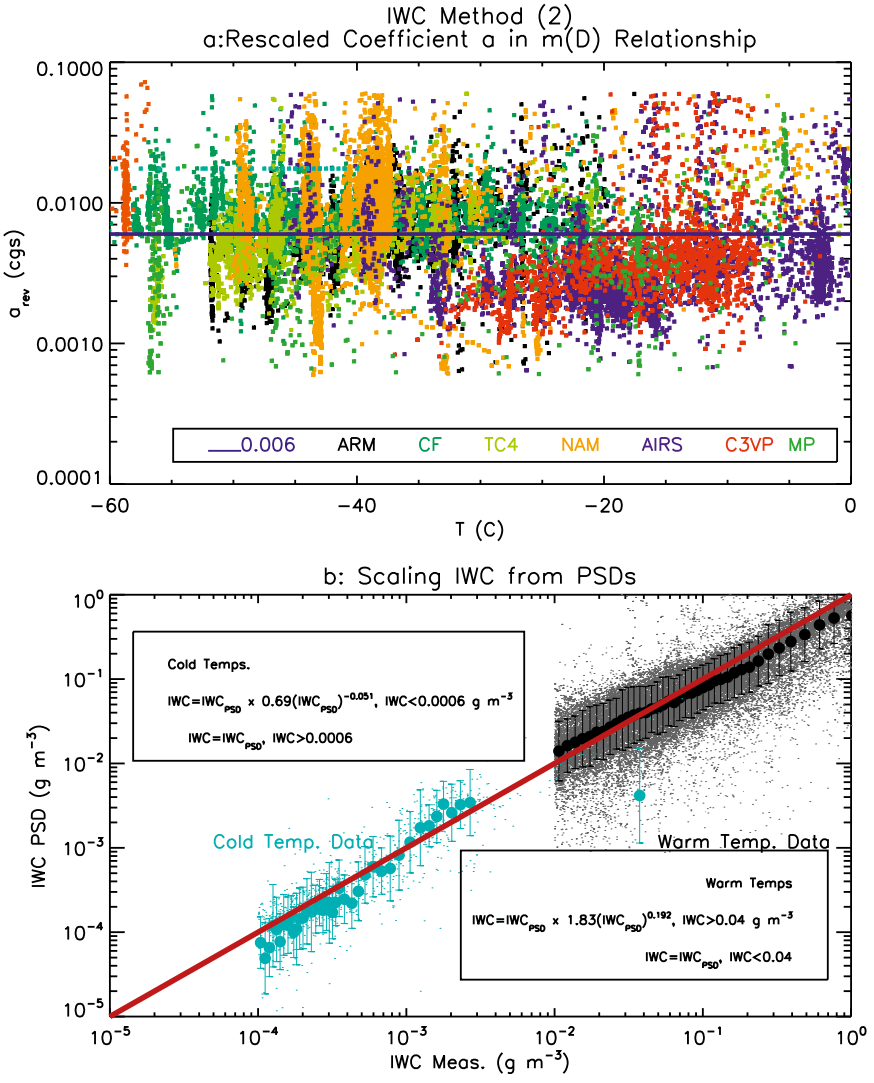

FIG. 3. Coefficient a in the mass–dimensional relationship $m = aD^b$ as a function of temperature for temperatures warmer than −60°C for IWC calculation method 2. (a) Rescaling is used to derive the a_{mod} coefficient that yields a match with the CVI IWCs, assuming that $b = 2.1$. (b) IWC derived from the PSDs compared to those measured, with curves fitted to the relationship over the IWC ranges indicated. Outside of those ranges, the relationship is assumed to be unity.

$m(D)$ relationship in (3), with coefficient $a = 0.006$ (cgs), close to the average of $a = 0.005\,28$ found by H10 from direct measurements of the IWC. An exponent of $b = 2.1$ in (3) is used for all of the warm-temperature field programs, because it is a representative "fractal mass coefficient" (H10). To estimate the IWCs for the particles below 50 μm, we used the gamma fits and evaluated the IWC contribution; it was generally only a few percent. For the lower-temperature observations, we use the power-law coefficients derived from the Schmitt and Heymsfield (2009) exponentially represented mass–dimensional relationships from above.

Set 2 calculates the IWC [(1)] using the values of a for the warmer- and lower-temperature observations (IWC_{PSD}) and then uses the measured IWC from the CVI probe:

$$a_{\text{mod}} = a(\text{IWC}_{\text{CVI}}/\text{IWC}_{\text{PSD}}). \tag{4}$$

In Fig. 3a for the warmer-temperature observations, there is a suggestion that a_{mod} in (4) is weakly temperature dependent. There is considerable scatter noted in the coefficient a_{mod}, and while most of the points are real, some points are attributable to CVI hysteresis when

entering and exiting cloud. Because of hysteresis, that single values of a do not give accurate masses, and because of the fundamental lower detection threshold of the CVI = 0.01 g m^{-3} for the warmer-temperature observations, set 2 uses the following approach to derive appropriate a_{mod} values. Figure 3b compares the measured and calculated IWCs for all of the observations. Curve fits are used to represent tendencies. Set 2 uses an a coefficient that is derived for each $\mathrm{IWC_{PSD}}$ multiplied by a relevant scaling factor (Fig. 3b).

Set 3 draws upon the concept that particle mass and area are related. Consider the area–dimensional relationship

$$A = cD^d, \tag{5}$$

where d is a power found from the data (discussed in section 3b). From a modeling study of fractal images, Schmitt and Heymsfield (2010) found that the mass–dimensional exponent b = constant × d, where the constant = 1.275 based on our more recent work. Thus, the 2D images of particles carry intrinsic information on their volumes and hence masses.

The different IWC calculation sets can be summarized as follows: set 1 is relatively simple because it allows an analytic function with prescribed (a, b) coefficients to yield particle masses; set 2 is superior to set 1 because it allows a determination of the (a, b) terms in the mass–dimensional relationship for each PSD. Set 3 allows us to evaluate whether our assumed (a, b) coefficients for set 2—especially b—are reasonable and incorporates information on the cross-sectional areas of the population representing a PSD, potentially enabling a self-consistent method to derive the terminal velocities of ice particle populations.

3. Results

This section presents (i) the results of the analysis obtained by fitting the PSDs to different functional forms and (ii) the relationship between particle cross-sectional area and temperature. The particle masses and cross-sectional areas are necessary inputs for (3) deriving ice terminal velocities.

a. Particle size distribution properties

We characterize the temperature variability of the total ice concentrations N_t, which represents the integration of the measured size-dependent concentration across the size distribution. The total ice concentration is the culmination of many processes including the activity of ice nuclei as a function of temperature, secondary ice production processes (e.g., Hallett–Mossop), ice depletion through aggregation downward in a cloud layer, transport upward in updrafts (e.g., NAMMA, warm clouds sampled during CF, gravity waves sampled during one CF cold-temperature case), and sedimentation from above. A discussion of why we believe that we are measuring most of the ice particles, given our 50-μm detection threshold for the observations at temperatures from 0° to −60°C, is given in appendix A. There are certainly exceptions (e.g., homogeneous nucleation in updrafts) at the base of ice virga.

The N_t values show wide variability at a given temperature (Fig. 4)—an expected result owing to inclusion of many different datasets. Residual artifacts from shattering also cannot be ruled out as a factor. There is a suggestion that N_t increases with temperature in the range from −86° to −60°C. The sample volumes of the probes used at temperatures below −60°C (except for the VIPS and a few replicator data points) are inadequate to provide reliable details of the decrease of N_t below −60°C. Thus, in light of this limitation we can assign the median value of about 27 L^{-1} to N_t below −60°C. For the warm-temperature observations, N_t (>50 μm) decreases by about an order of magnitude roughly exponentially as temperature increases from about −60° to 0°C. The values of N_t are considerably above the Demott et al. (2010) average ice nucleus (IN) concentration–temperature relationship for these warmer temperatures. Convection is partially responsible for the variability. For the convective cloud cases, the fitted relationship is $N_t = 9.7e^{-0.026T}$ and for the stratiform cases, it is $N_t = 3.1e^{-0.049T}$; convective cases have a larger intercept parameter and flatter slope. We suggest that the IN concentration alone is not a good predictor of ice concentrations at a given temperature in mature ice clouds.

Figure 5 is used to characterize the changes in the properties of the PSDs with temperature and by whether the clouds are designated as convective or stratiform in their formation mechanisms. The curves represent average concentrations found in a given size bin when one or more particles are detected in a given (5 s) PSD, thereby factoring out when no particles are sampled. The PSDs clearly broaden with temperature and the convectively generated clouds have broader PSDs than the stratiform ones.

The size of the largest measured particle in the PSDs (D_{max}) clearly indicates the trend noted in Fig. 5. The values of D_{max} increase from 20 μm at the coldest temperatures to about 1 cm at the warmest ones (Fig. 6, shown as median values). The largest particles in the convective cases are about twice those in the stratiform cases (Fig. 6). Curves fitted to the D_{max} versus temperature plots further highlight the differences between the two categories (Fig. 6).

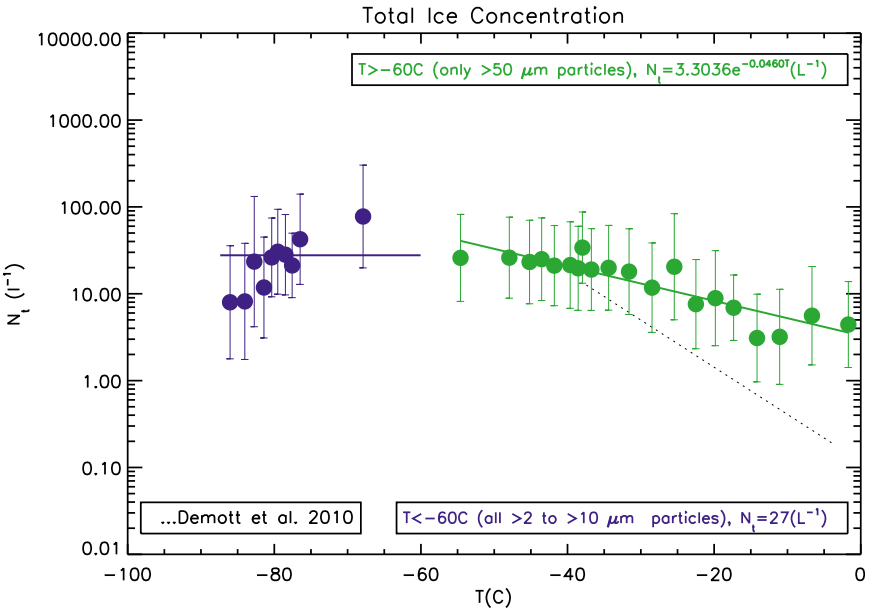

FIG. 4. Total ice number concentrations above sizes 2–10 μm for $T < -60$°C (blue), depending on the field program, and approximately 50 μm for $T > -60$°C (green). Median values of N_t in increments of equal numbers of data points are plotted through the data for each size range. The average curve developed by Demott et al. (2010) is shown by the dotted line.

We now examine the general properties of the PSD functional forms by fitting them to gamma functions of the form

$$N(D) = N_0 D^{\mu} e^{-\lambda D}, \tag{6}$$

where N_0 is the intercept, μ is the dispersion, and λ is the slope. The fit parameters are derived using a moment-matching method that favors the first, second, and sixth moments of the PSD (Heymsfield et al. 2002) and particles are considered from 10 μm or below to about 0.3 mm for $T < -60$°C and 50 μm up to 1 cm or larger for $T > -60$°C.

The $D_{\max}$ values are related to λ, with the broadest PSDs (smallest λ) occurring with the largest particles (Fig. 7a) and correspondingly smallest N_0 (not shown). There is a downward trend in $D_{\max}$ noted from the warmer to the colder temperatures. Below about −60°C, there is a downward shift in $D_{\max}$. This shift could be due to our restriction of the largest particles in the SCOUT PSDs to be 200 μm to reduce the chances of shattering of large particles artificially enhancing the FSSP observations, although few such instances occurred; extrapolation of the curve developed for above −60°C to lower temperatures probably would accurately represent the true $D_{\max}$.

The decrease of λ with temperature (Fig. 7b) has been found in many earlier studies (Houze et al. 1979; Heymsfield 2003, hereafter H03). Our λ values tend to be lower at a given temperature than those found in earlier studies, because we have filtered our 2D probe data to reduce the number of small shattered particles that tend to raise the λ values (Heymsfield et al. 2008). Smaller values of λ are noted for a given temperature in the convective cases than in the stratiform cases. Relationships have been fitted between the various combinations of data (Fig. 7b).

Appreciable differences in the λ–T relationships are noted by field program, as is best illustrated by exponential fits of the form $\lambda = a_\lambda e^{b_\lambda T}$ to the λ–T data (Figs. 8a–g) and as summarized in Fig. 8h. The intercept values at a temperature of 0°C (a_λ; Fig. 8g) tend to be smaller for the convective (Figs. 8b–d) than for the stratiform clouds, reflecting the broader PSDs for the former. The decrease in λ with temperature is steeper in the convective than stratiform cases (larger negative b_λ). We suggest that in the convectively generated clouds, where the value of b_λ is strongly negative, there is new nucleation with decreasing temperature in the updrafts. The dependence is also enhanced by ice concentrations reduced at the warmer temperatures by aggregation because of the presence of more ice mass than in the stratiform clouds. (The CVI median and mean IWC are 0.096 g m^{-3} and 0.24 ± 0.35 g m^{-3} for the convective clouds and 0.039 g m^{-3} and 0.09 ± 0.14 g m^{-3} for the stratiform clouds).

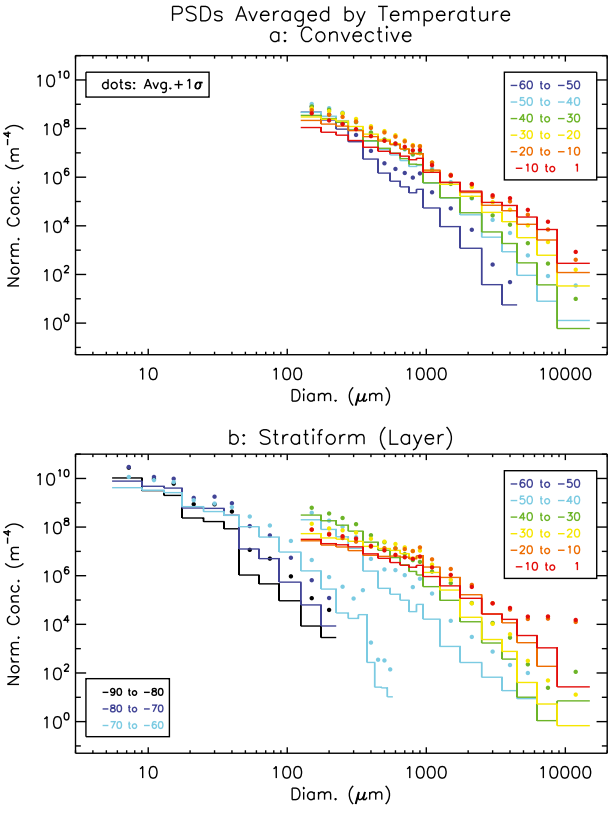

FIG. 5. Average size distributions plotted in 10°C increments from −90° to 0°C, separated into the two classes: (a) convective and (b) stratiform. The dots show one standard deviation above the average value/bin. Details of the PSD averaging are described in the text.

There is a direct relationship between μ and λ (Fig. 9a)—a feature that has been explained by Zhang et al. (2003) for raindrops. Values of μ are between -1 and 1 for λ values between about 20 and 100 cm^{-1} for both the stratiform and convective cases over a wide range of PSD slopes. Below $\lambda = 20\,\text{cm}^{-1}$, μ values are primarily between -1 and the theoretical lower limit $\mu = -2$, indicating a superexponential PSD shape and indicating that the assumption of exponentiality at the warmer temperatures is not appropriate. Curves fitted to the μ versus λ relationship using different ways of combining the observations are shown. For computational reasons though, we suggest that a limit be placed on μ of -1.

With temperature, μ values are generally between -1 and 2 for temperatures above -60°C, indicating that the PSDs straddle exponential at these temperatures (Fig. 9b), more so for the stratiform than the convective cases. Appreciably higher-than-exponential values of μ are noted for temperatures below -60°C, signifying lower concentrations of the smaller particles than given by exponentials.

We can evaluate how accurately the PSD-fitted parameters yield the IWC. Integrating the gamma PSD form of the PSDs with the power-law representation $m = aD^b$ from 0 to ∞ yields

$$\text{IWC}(\text{g m}^{-3}) = aN_0 \times 10^6 \Gamma(b + \mu + 1)/\lambda^{(b+\mu+1)}. \quad (7)$$

The IWC calculated using the PSD-fit coefficients (cgs units) and the (a, b) coefficients from set 1 is compared to the corresponding measured IWC in Fig. 10. On average for the warmer-temperature observations, the IWCs are overestimated at low values of the IWC (Fig. 10a), in part because the use of a single $m(D)$ relationship in (7) gives masses higher than that for solid ice spheres for sizes below 45 μm (although incomplete gammas could be used). For the higher IWCs, on average (7) produces underestimates, because most of these are from convective situations where riming produces higher values of a than used (H10). For the lower-temperature observations, (7) gives good results (e.g., Fig. 10b). Overall, the IWCs are accurately described using the PSD-fitted form, but improvements are found when (a, b) coefficients for sets 2 and 3 are used (not shown).

b. Particle area

Particle cross-sectional area normal to the fall orientation of an ice crystal A is a necessary input into calculations of the terminal velocity V_t, which is the focus of section 4. We use area measurements derived from the 2D probe data for each particle for the warmer clouds. For the colder clouds where we use our small particle probe data, we the $A(D)$ relationships from the PreAVE and CF VIPS data from Schmitt and Heymsfield (2009) for those cases and SCOUT and the Replicator observations (Miloshevich and Heymsfield 1997; Heymsfield and Miloshevich 2003). The 2D and Replicator images are views of particles in approximately their fall orientation (but not for the VIPS). We did note that some particles are oriented by the flow field around the probe as they are sampled—an effect pointed out by King (1986)—but in that study the particles were pristine and reorientation because of elongation (needles) or reorientation (thin plates, dendrites) was more pronounced than expected here.

The area ratio A_r given by the ratio of the particle area divided by the area of a sphere that completely encloses the projected area of a particle,

$$A = A_r(\pi/4)D^2, \quad (8)$$

is found for every particle imaged.

For temperatures above -60°C, an average A_r value is found for each size bin of each 2D PSD and then fit to the form

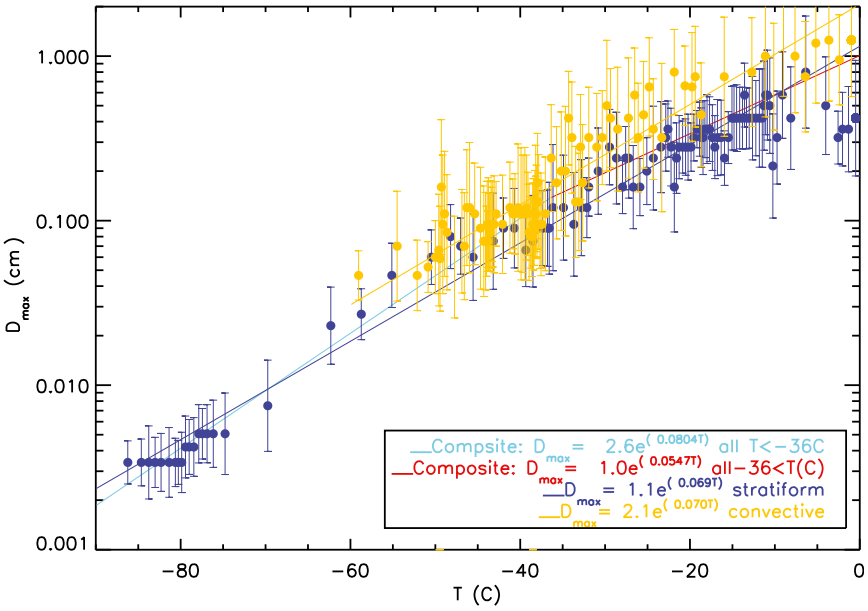

FIG. 6. Maximum diameter in each PSD as a function of temperature, shown as median values in temperature intervals given by an equal number of points as derived from the individual PSDs as a function of temperature; median values shown separately for $T < -60$°C and $T > -60$°C. Exponential curve fits to the field program data identified as convective clouds, stratiform clouds, and for all clouds combined are shown.

$$A_r = \alpha D^{\beta}. \tag{9}$$

Below −60°C, the Replicator images are used to derive α and β for that dataset and a single power-law representation of the Schmitt and Heymsfield (2009) combined exponential and power-law fits to different size ranges is used.

The values of α increase with temperature from −60° to 0°C (Fig. 11a). This increase as the temperature increases toward 0°C indicates that the particles are increasingly filled in, possibly reflecting a trend from more pristine particles (e.g., columns, bullet rosettes) at low temperatures to aggregates and more complex 2- and 3D forms at warmer temperatures. Similarly, the value of β approaches 0 as temperature increases from −60° to 0°C, thus indicating a value decreasing toward that of a sphere (Fig. 11b). These trends are reflected in the nearly monotonic relationship between α and β (Fig. 11c), with increasing values of α associated with increasing β and thus more of a tendency for filled in particles at the larger β values.

The value of β is the approximate fractal particle dimension (Falconer 2003), and we can use this value to assess how well the exponent of 2.1 used in the $m(D)$ relationship fits with the value of $b = 2.1$. This is the value of the exponent we use for our IWC calculations via (a, b) sets 1 and 2 discussed earlier. Here, d in set 3 is given by $d = \beta + 2$, and the power b in the mass–dimensional relationship is given by $1.275d$. There appears to be a linear increase in the value of b over the −60° to 0°C temperature range. The value of $b = 2.1$ provides a good average throughout the range, although the use of the temperature variability of b would improve the comparison of measured and calculated IWCs as was done in Schmitt and Heymsfield (2010).

With knowledge of the fractal value of b for each PSD, coefficient a can then be found. This is done by using the gamma PSD-fit coefficients, the measured value of the IWC, and the parameterized form of the PSDs (6) rather than the PSDs themselves for simplicity. The value of a increases with temperature, largely as a result of the trend noted for b (Fig. 12). The choice of $a = 0.006$ (cgs) fits the data quite well throughout the −60° to 0°C temperature range.

c. *Terminal velocities*

Heymsfield and Westbrook (2010) developed a relationship for deriving ice particle V_t, as a function of particle mass and area ratio, temperature, and pressure, based on laboratory tank experiments. By accounting for the area ratio directly, this approach produces more accurate terminal velocities than from earlier methods. Using this relationship together with the more accurate masses from the (a, b) coefficients in set 2, we derived V_t

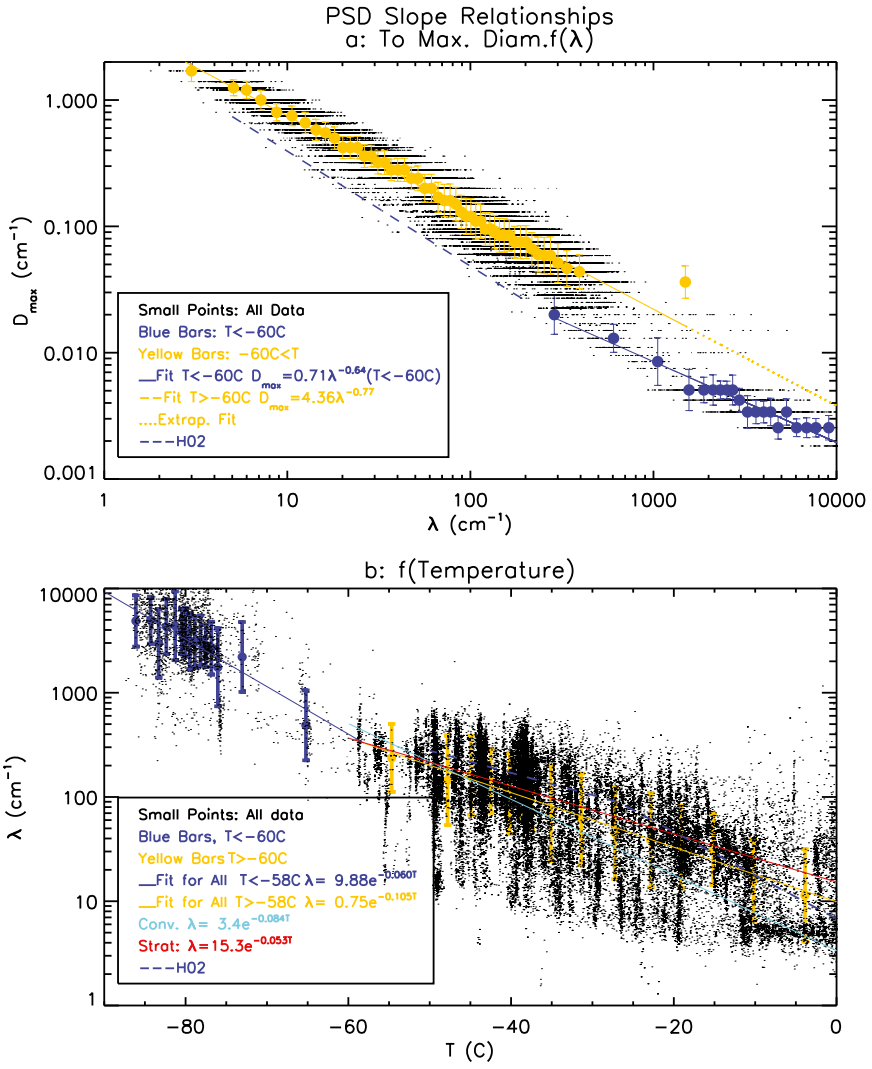

FIG. 7. Slope λ of gamma size distributions fitted to 5-s 2D imaging-probe spectra, except for $T < -60$°C, where FSSP+2D, VIPS, or Replicator PSDs are used. (a) Relationship between PSD maximum diameter and λ, and (b) λ as a function of temperature. Various fits to the data, partitioned in different ways, are shown.

representing the particles sampled in our study. Examples of V_t as a function of D for each field campaign are shown in Fig. 13.

Most relationships developed to represent $V_t(D)$ from data or calculations are presented in a power-law form, usually for a pressure level P or air density ρ_a of 1000 hPa. Adjustments of this relationship to other pressures and temperatures take on the following forms (Rutledge and Hobbs 1984; Lin et al. 1983):

$$V_t = aD^b(1000/P)^w \quad \text{or} \tag{10a}$$

$$V_t = aD^b[\rho_a(P = 1000\,\text{hPa})/\rho_a(P)], \tag{10b}$$

where $w \sim 0.4$. Because the temperature at level P is not known and use of a standard atmosphere would give a temperature above 0°C, we use the formulation given by pressure [see (10a)] in the following discussion. The ratio $\rho_a(1000)/\rho_a(P)$ in (10b) is approximately the ratio of pressures in (10a). For example, the factor of 2.0 ratio using P from 1000 to 500 hPa is a density ratio of 1.85 when the temperatures are 0° and −20°C, respectively.

In practice, V_t relationships are often extrapolated to sizes well beyond the range for which they were derived. For example, the widely used relationship of Locatelli and Hobbs (1974) is plotted in Fig. 13. It was derived for unrimed radiating assemblages of dendrites and aggregates of dendrites with a size of 0.2–1.0 cm, as indicated

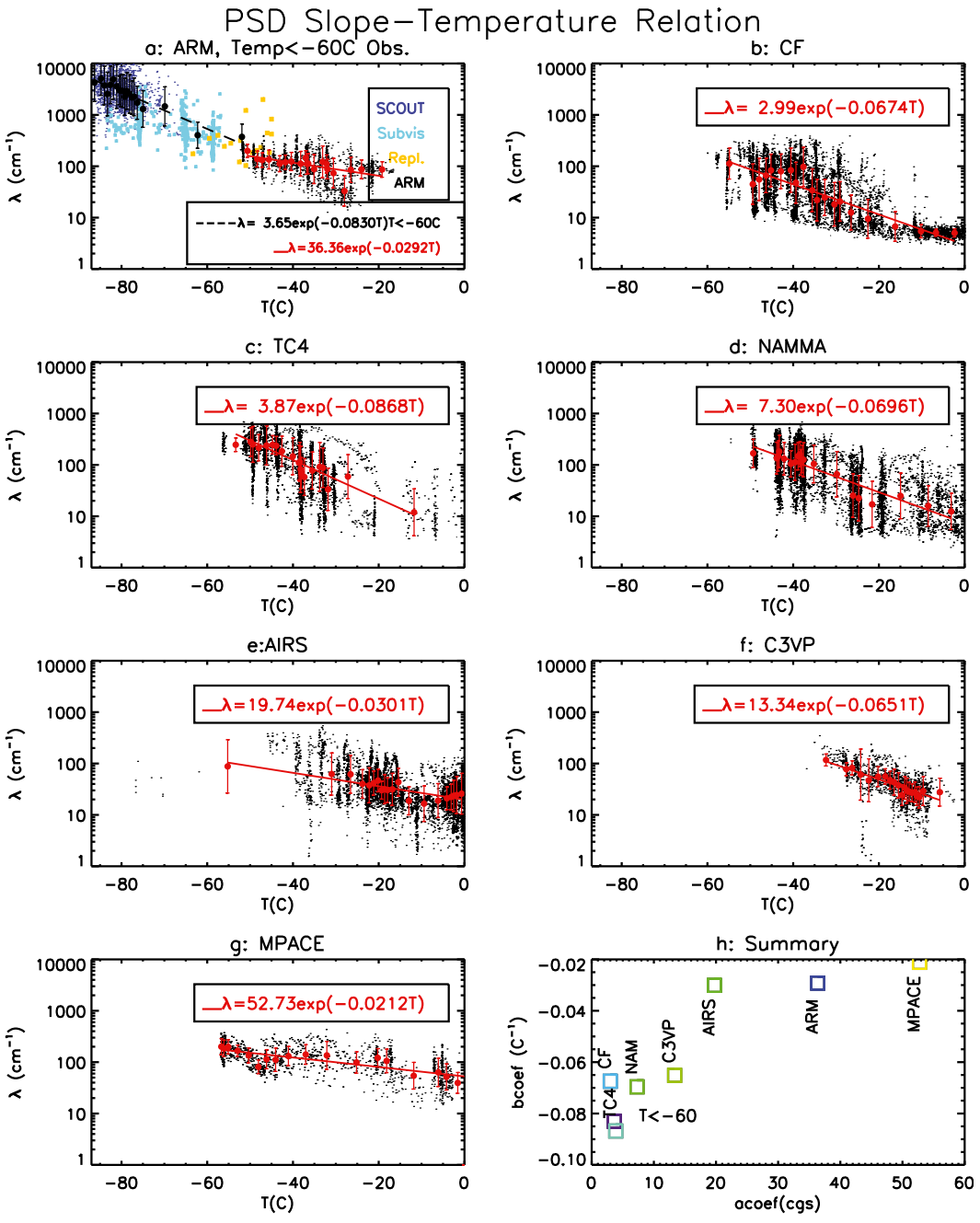

FIG. 8. (a)–(g) Slope λ of gamma PSD fitted to the 5-s PSDs as a function of temperature for the various field campaigns; cold-temperature data shown in (a). Exponential curve fits of the form $\lambda = a_\lambda \exp(b_\lambda T)$ were fitted to the data and are listed. (h) Exponential fit coefficients a_λ and b_λ for the various field campaigns are plotted, except for the low temperature observations, where the median values of the coefficients are shown.

in the article, but it is often used to cover the full range of sizes required for the calculations. Mitchell (1996) was careful to note this point. Other relationships may cover a wider range of sizes (e.g., Ikawa and Saito 1991; Fig. 13) but are not appropriate for the full range of sizes needed for calculations, and, as we show, the pressure adjustment may not be appropriate. As shown from our calculated V_t values in Fig. 13, a power-law form, which would appear as a straight line in Fig. 13, is often not appropriate for use over the full range of sizes in a PSD.

An implicit assumption in earlier studies is that particles of all sizes contribute to the total precipitation

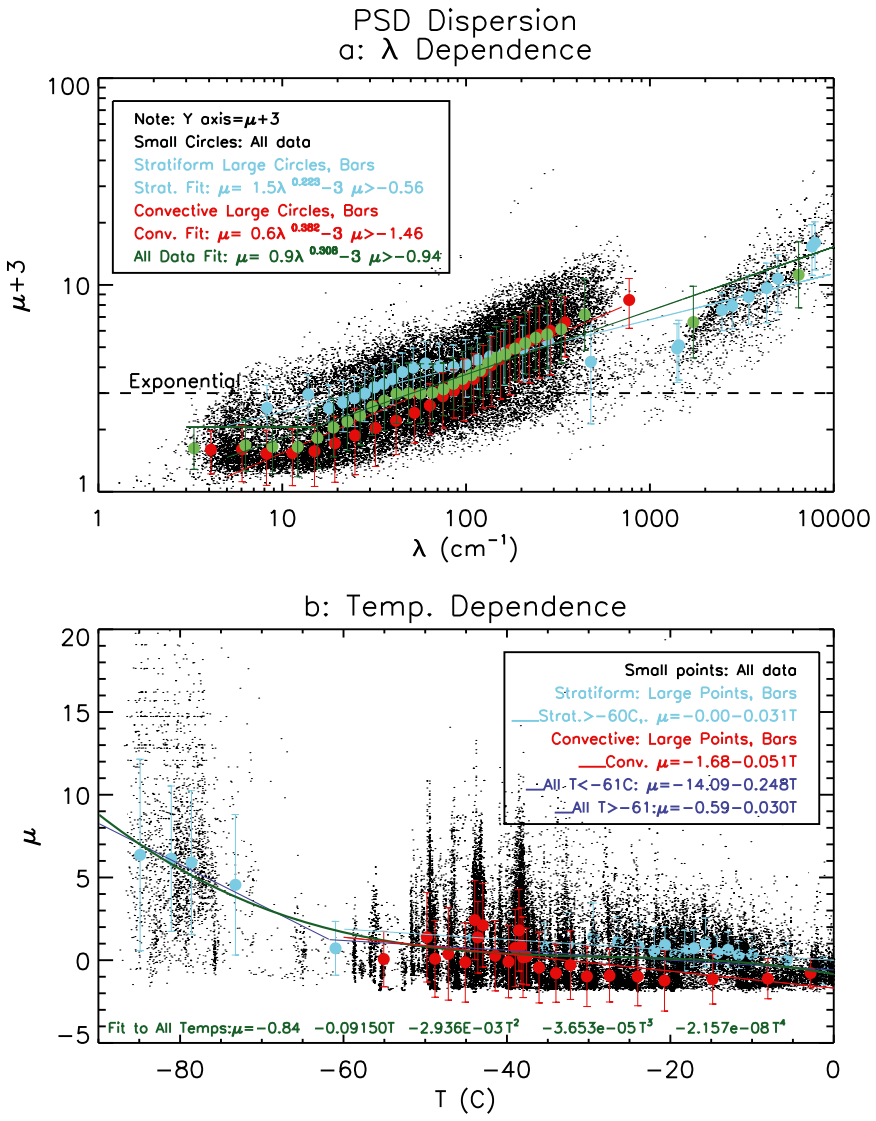

FIG. 9. PSD dispersion μ as a function of (a) slope and (b) temperature. In (a), note that the scale for μ adds a value of 3 to the derived value so that the plot can be made on a logarithm (y axis) scale, and the dashed horizontal line corresponds to an exponential PSD, where the gamma PSD has a value of $\mu = 0$. The term cc is the goodness of fit of the PSDs.

rate—a premise that produces considerable error in snow precipitation rates, especially when a V_t–D power-law-type relationship is extrapolated well beyond its measurement range. Accordingly, we use a new and more objective technique to develop V_t–D relationships. Using $m(D)$ relationships appropriate for each PSD from set 2 and the fitted $A_r(D)$, we use the term inside the summation of (1) to derive the distribution of the IWC per size bin across the PSD and the total IWC. The measured PSDs rather than the fitted ones are used to maximize the accuracy of finding the dominant IWC contributors. Examination of the bin size–dependent contribution to the IWC reveals that it is not uniformly distributed across all sizes but rather is a distribution with a clearly defined peak somewhere near the mid-diameter of the PSD (Fig. 13; see plus signs).

We employ the following approach to reduce potential errors in developing a V_t–D relationship. For each PSD, we find the bin diameter at the peak of the IWC (D)–D distribution and then find the diameter range either side of the peak that yields 70% of the total IWC [crosses on either side of the peak (plus sign) in Fig. 13]. The quantitative amount of 70% is chosen arbitrarily, but it is well within the diameter range where the V_t–D relationship can be represented reliably with a power-law form (corresponding curve plotted in each panel).

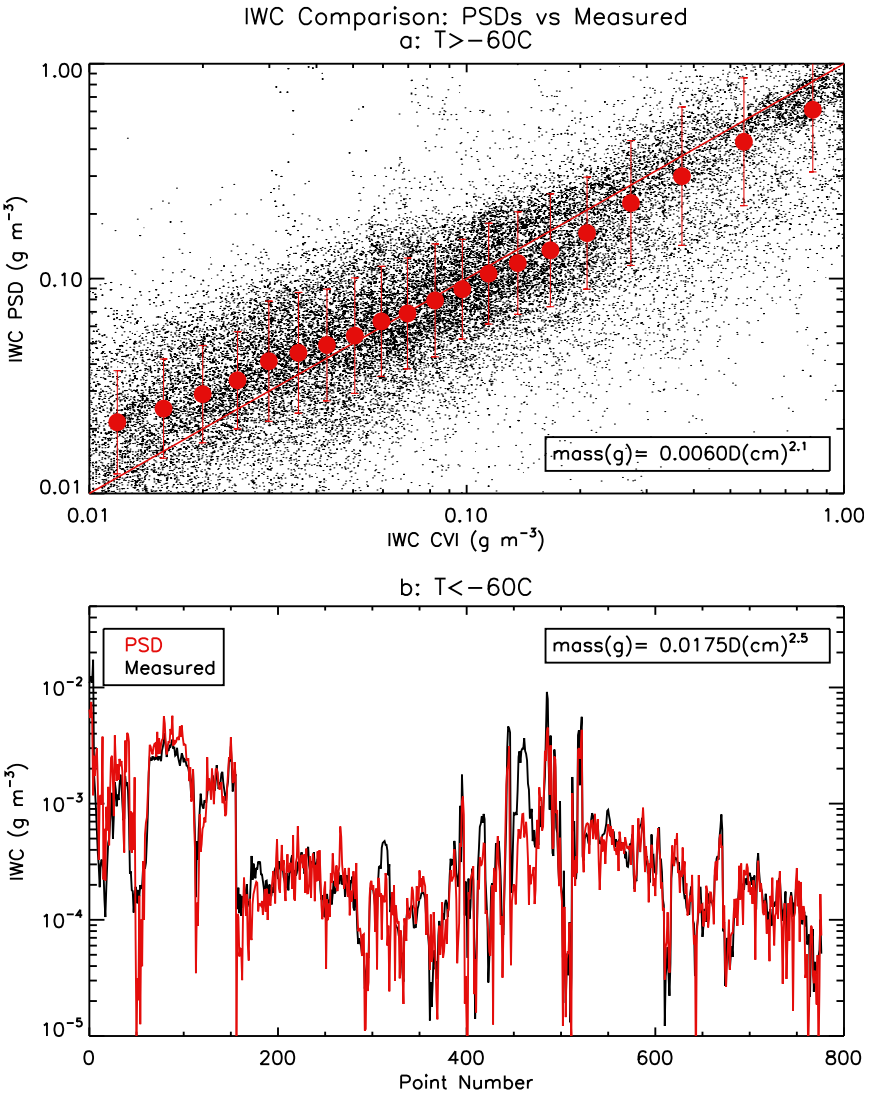

FIG. 10. (a) Comparison of the IWC derived from the PSDs with one assumed mass–diameter relationship (shown) to those measured by the CVI, for the data at temperatures −60°C and above. (b) IWCs calculated from the PSDs and $m(D)$ relationship from Schmitt and Heymsfield (2009), for data at temperatures below −60°C.

The range of sizes producing 70% of the total IWC is much smaller for the lower-temperature cases than for the higher ones (Fig. 13). For the small particles, the V_t approaches the values for Stokes ice spheres, as expected but falls well below an extrapolation of the LH74 curve used in many models (Fig. 13). The fall velocities of the larger particles in the convectively generated clouds tend to be larger than for in situ–generated clouds for the same diameter (Fig. 13) because the masses are higher than in the stratiform situations.

The range of sizes producing most of the IWC increases with decreasing PSD slope (Fig. 14a), with differences noted between the values for the various field campaigns. The upper size of the 70% range approaches the maximum diameter of the PSD, especially when this maximum size is hundreds of microns rather than centimeters (Fig. 14b).

Adjustment of terminal velocity from sea level to a given atmospheric pressure is necessary to estimate fall speeds aloft accurately. Using a single value for w in (10) of 0.4 or 0.5 (e.g., Lin et al. 1983), the adjusted V_t values for given pressure levels were compared to the values derived more accurately using the Heymsfield and Westbrook (2010) relationship (Fig. 14c). The resulting errors can be appreciable—up to 60% for small particles.

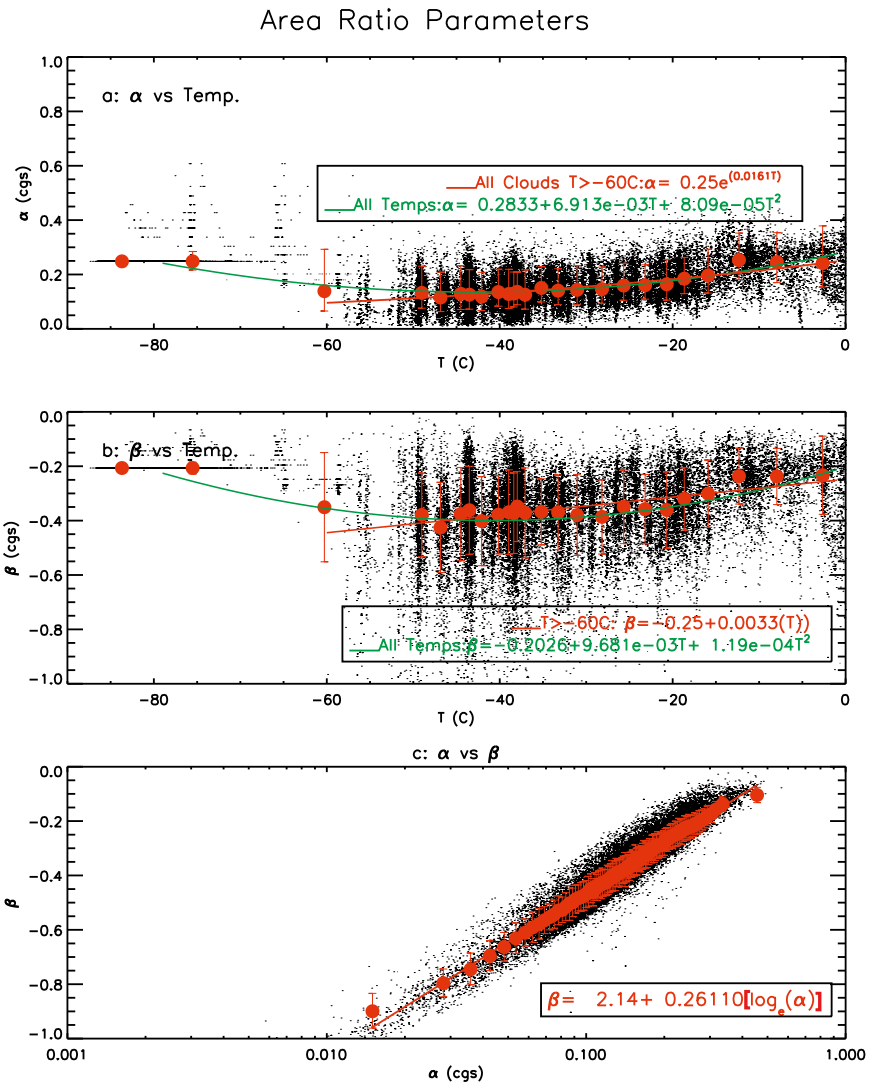

FIG. 11. Coefficients in the area ratio–size relationship given by the form $A_r = \alpha D^{\beta}$, where D is in centimeters, as a function of temperature: (a) α, (b) β, and (c) the relationship between the two parameters. Curve fits to the data are shown.

We can compile a dataset of the V_t values for those particle sizes that contribute 70% of the total IWC for each field program and derive them for a common pressure of 1000 hPa to compare further our observations to those of LH74 and to each other (Fig. 15). Although we could have considered 70% of the IWC and total particle area in developing the relationships, this process works well for the warmer temperatures where both parameters fall in about the same range of sizes and for the lower temperatures the smaller particles behave as Stokes particles. The V_t value for particles in the 500- to about 3000-μm size range for the stratiform cases corresponds quite closely to LH74 in their measurement size range of 2–10 mm but underestimates them by a factor of 2 or 3 for the convectively generated ice.

Using the 70% IWC criteria to define the important range of V_t values for climate studies, the V_t values for four pressure levels—1000, 800, 600, and 400 hPa, representing the range corresponding to sea level and most ice cloud heights—have been derived. The motivation is to develop V_t–D relationships that can be readily adjusted to include pressure levels for most subfreezing cloud temperatures. Figure 16 shows the results for pressure levels of 400 and 800 hPa, partitioned by convective and stratiform cloud types. Several power-law-type curve fits are included over size ranges where these fits are well represented by power-law relationships: sizes smaller than 40 μm where $V_t \sim D^{2.0}$, intermediate sizes where $V_t \sim D^{0.9}$, and large sizes where $V_t \sim D^{0.2}$. The flatness of the curve for the largest size range is consistent

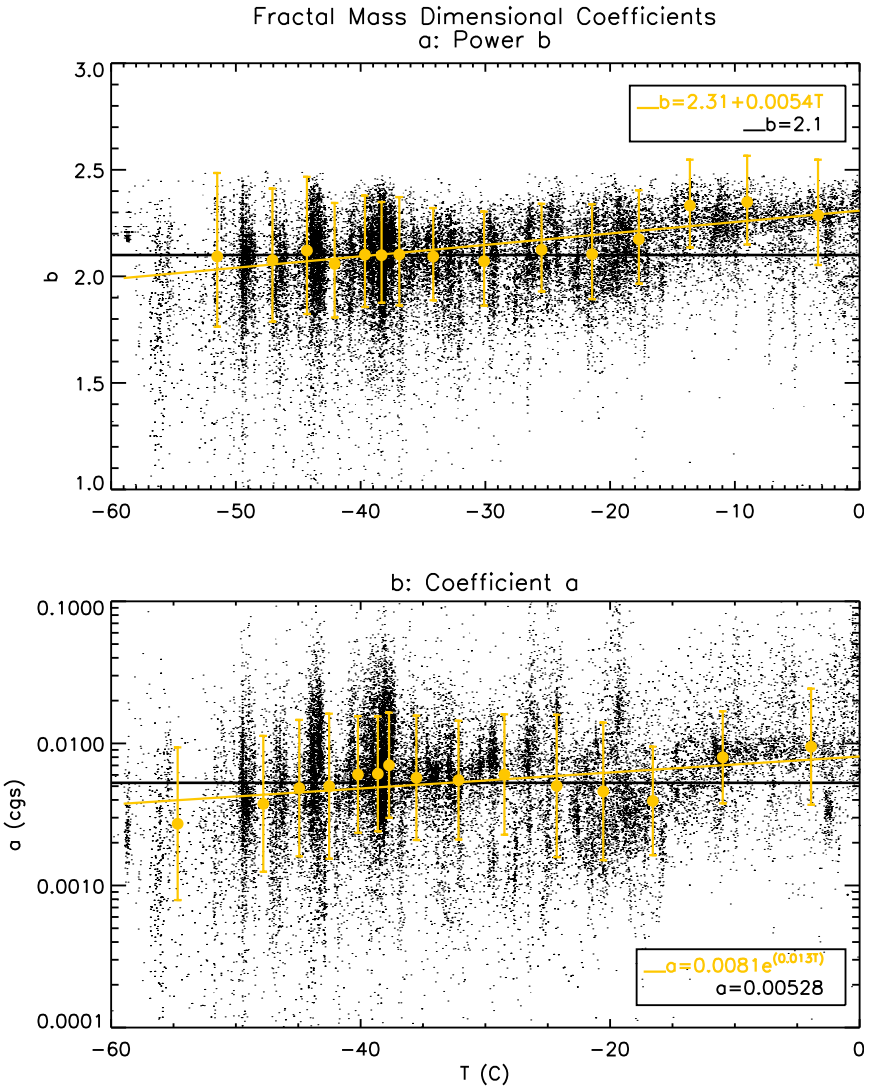

FIG. 12. (a) Coefficient b in the mass–dimensional relationship as derived from the fractal relationship to the area ratio coefficient β (see text) for the data at temperatures −60°C and above. (b) Using coefficient b from (a), the corresponding a coefficient that yields the measured IWCs. A fit to the data is shown. In (a) and (b), reference values for the calculated IWCs used in Fig. 10a are shown.

with earlier measurements, indicating that the fall speeds are relatively constant with size for aggregates with $D >$ 1 mm (e.g., LH74 with $b = 0.16$). The smallest size range corresponds to Stokes-size particles. In this range, the ratio of the prefactors in the relationships at the two pressures (0.0032/0.0028 = 1.14) is much smaller than the value given by (16) with $w = 0.4$ or 0.5, mirroring the findings from Fig. 14c that there should be very little pressure adjustment for small particles. The overcompensation for pressure effects on V_t extends to sizes up to 1 mm. This is an extremely important point because a single exponent dependence would yield fall speeds for $D < 1$ mm that are too large and would yield decreased ice cloud lifetimes in models, especially for cold clouds. A more accurate pressure adjustment scheme and a reliable non-power-law relationship covering all size ranges are clearly warranted.

The results shown in Fig. 16 can be generalized by developing V_t–D power-law-type relationships fitted over different intervals of D as in Fig. 16, for a pressure level of 1000 hPa, and then by factoring in a multiplicative pressure-dependent correction term. For certain applications, it is desirable to have a single polynomial fit to all sizes, and this function has also been derived.

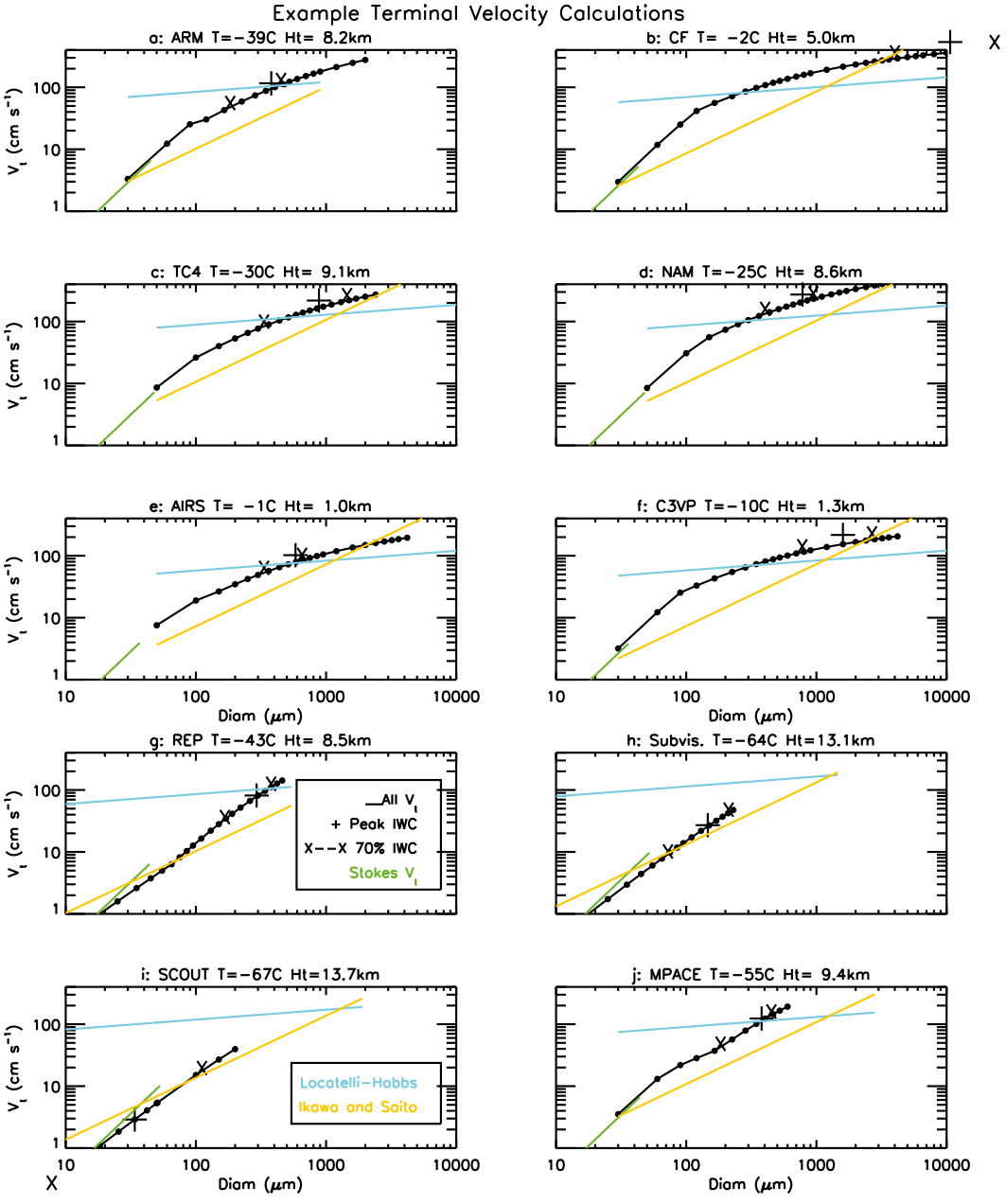

FIG. 13. Calculated terminal velocities as a function of particle diameter for one example PSD for each of the 10 field programs. In each example, the pressure at the PSD measurement level is used to derive the V_t values and is also used to adjust the values shown for the Locatelli and Hobbs (1974) curve according to an enhancement factor $(1000/P)^{0.4}$. The symbols represent different assumptions, as described in the text.

For a pressure level of 1000 hPa, for designated stratiform clouds, the following relationships are developed:

$$V_t(\mathrm{cm\,s^{-1}}) = -0.0028D^{2.00}, \quad D < 41\,\mu\mathrm{m}, \tag{11a}$$

$$V_t = 0.0791D^{1.101}, \quad 41 < D < 839\,\mu\mathrm{m}, \quad \text{and} \tag{11b}$$

$$V_t = 62.29D^{0.1098}, \quad D > 839\,\mu\mathrm{m}, \tag{11c}$$

or for one representation,

$$V_t = 10^{\sum_{i=0}^{3} q_i(\log_{10}D)^i}, \tag{11d}$$

where $q_{(i=0\text{to}4)} = -3.226,\ 3.466,\ -0.6965,\ 0.044\,00$ (range of applicability $2 < D < 10\,000\,\mu$m), for designated convective clouds:

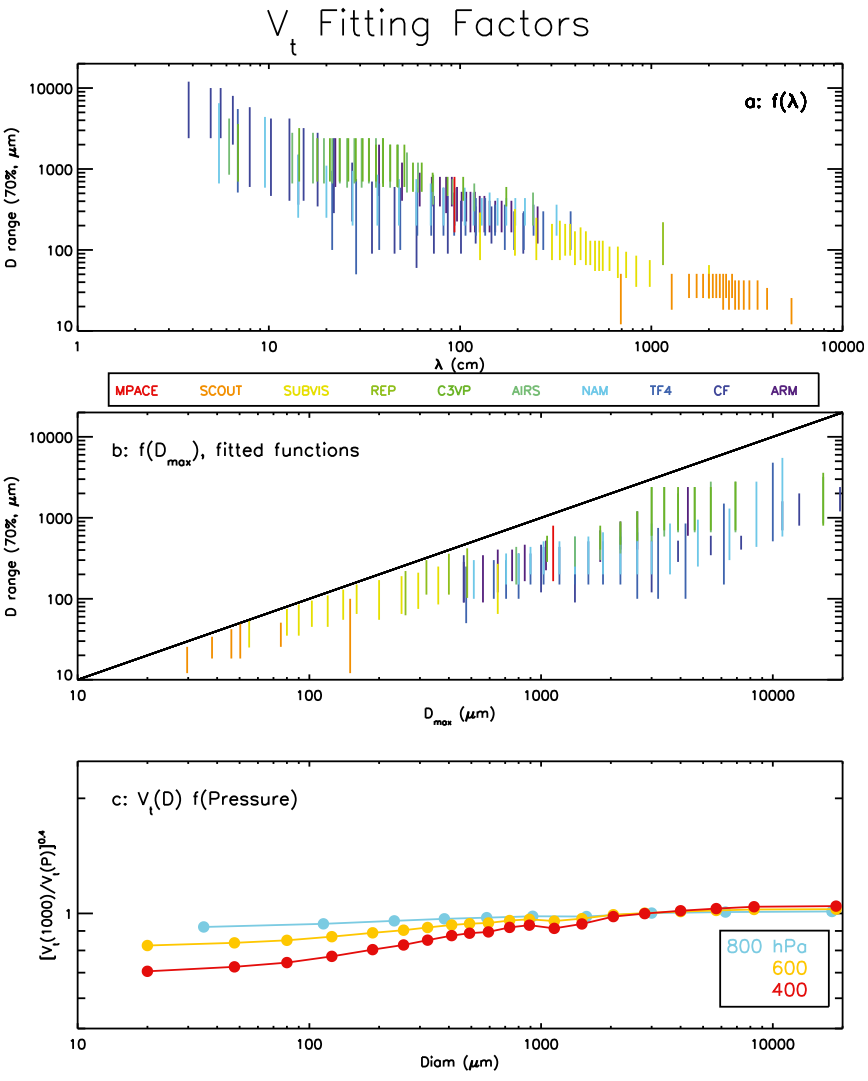

FIG. 14. Properties of the distribution of terminal velocities with size based on the measured PSDs. (a),(b) Range of particle sizes that contribute to 70% of the total IWCs (see plus signs in Fig. 13), centered around the peak in the distribution of IWC (crosses in Fig. 13) for each PSD, for all PSDs combined, (a) as a function of the PSD slope and (b) as a function of the largest particle measured in each PSD. (c) Ratio of correction in V_t for pressure levels corresponding to the measurements as a function of particle diameter, assuming the power in the correction is 0.4, for pressure levels of 800, 600, and 400 hPa. Median values are shown in intervals of D.

$$V_t(\mathrm{cm\,s^{-1}}) = 0.0028D^{2.00}, \quad D < 56\,\mu\mathrm{m}, \tag{12a}$$

$$V_t = 0.1194D^{1.0697}, \quad 56 < D < 640\,\mu\mathrm{m}, \tag{12b}$$

$$V_t = 21.90D^{0.2629}, \quad D > 640\,\mu\mathrm{m}, \quad \text{and} \tag{12c}$$

$$V_t = 10^{\sum_{i=0}^{3} q_i(\log_{10}D)^i}, \tag{12d}$$

where $q_{(i=0\text{to}4)} = -4.449,\ 5.138,\ -1.3748,\ 0.130\,57$ (range of applicability $2 < D < 10\,000\,\mu$m).

Assuming pressure levels of 800, 600, and 400 hPa, we derived the pressure correction term relative to a pressure of 1000 hPa (Fig. 17a) and represented it in the following analytic form (Fig. 17a):

$$V_t(P)/V_t(1000) = C_0 + C_1 \ln(D). \tag{13}$$

Note that the pressure correction is size dependent and again is much below the non-size-dependent corrections (for all sizes) used in earlier studies. Also, the terms C_0 and C_1 in (13) are each pressure dependent.

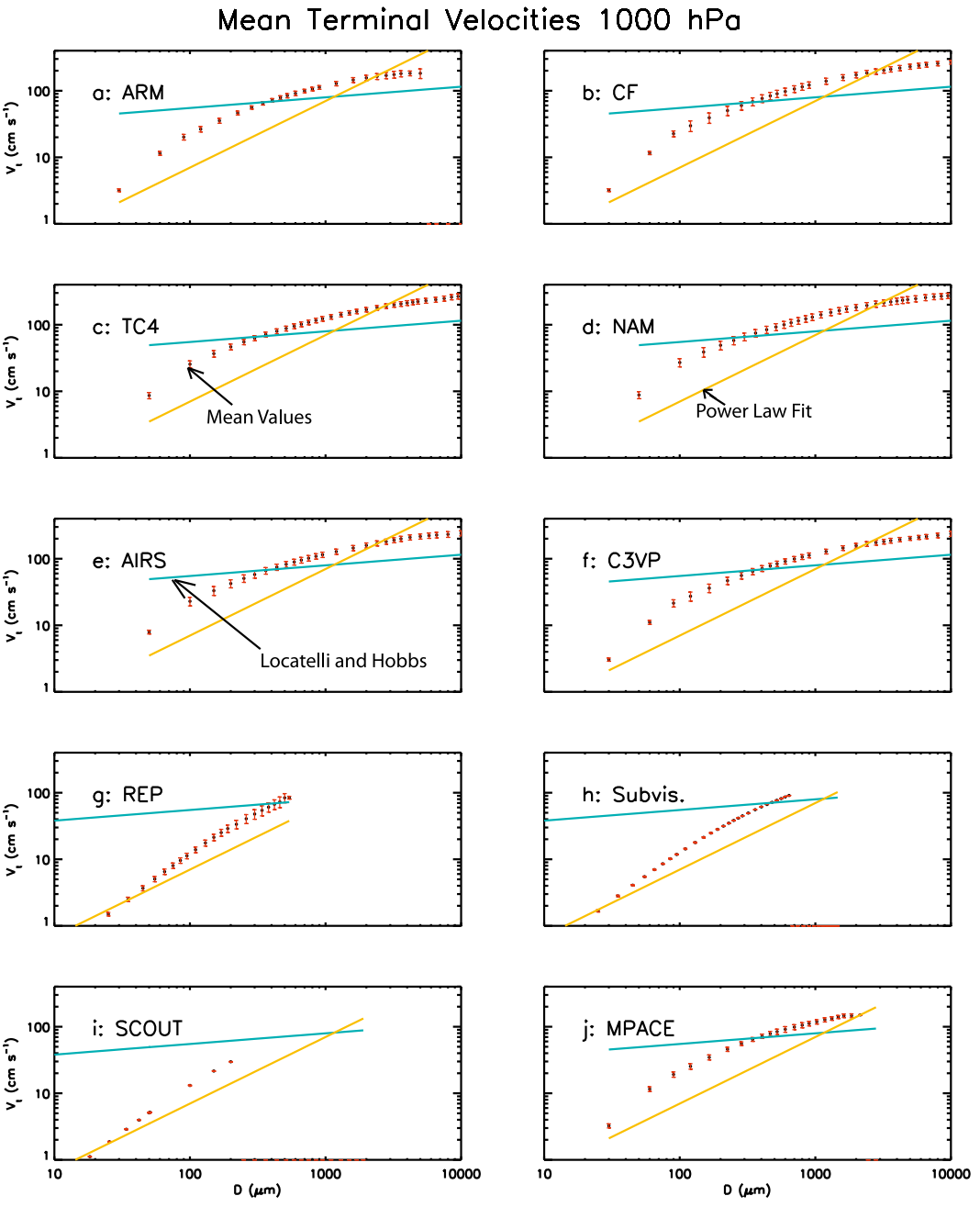

FIG. 15. Mean terminal velocities as a function of particle size, assuming a pressure level of 1000 hPa for each of the field campaigns. Locatelli and Hobbs (1974) relationship is shown for reference.

Drawing upon the curve fits in Fig. 17a, Figs. 17b and 17c are used to derive a single pressure-dependent correction C that is multiplied by the $V_t(D)$ in (11) and (12),

$$C = C_0(P) + C_1(P)\ln(D), \tag{14}$$

where in Figs. 18b and 18c we derive the following analytic terms:

$$C_0 = -1.04 + 0.298\ln(P) \quad \text{and} \tag{15}$$

$$C_1 = 0.670 - 0.097\ln(P). \tag{16}$$

These curves are plotted on top of the $V_t(P)/V_t(1000)$ values for the ensemble of data points and fit the data quite well, except at the lowest sizes and largest sizes where the curves have to be truncated. Particles of Stokes

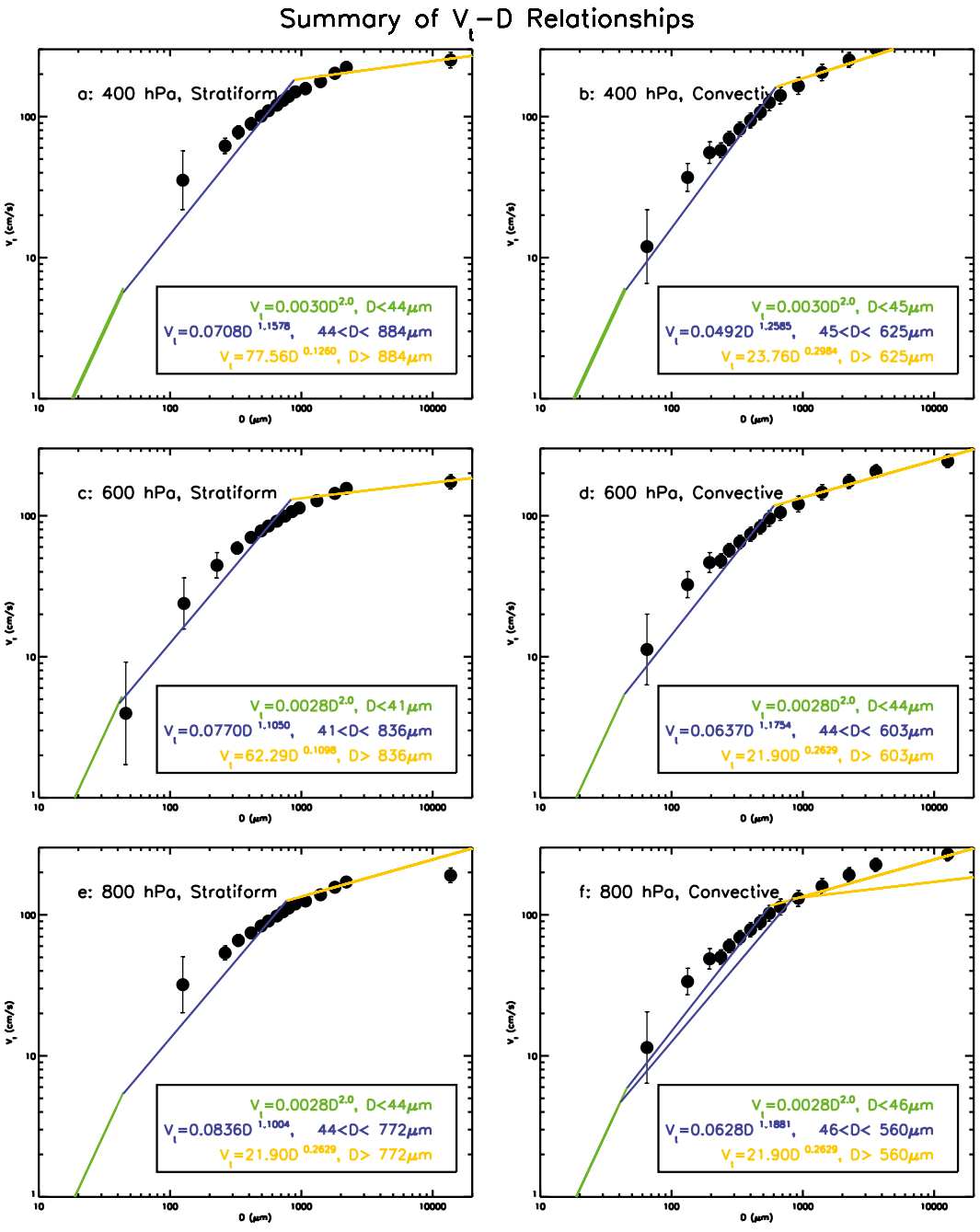

FIG. 16. Average terminal velocities as a function of particle diameter for (a),(c),(e) stratiform and (b),(d),(f) convectively defined ice clouds, and pressure levels (top) 400, (middle) 600, and (bottom) 800 hPa. Power-law relationships are fitted to the calculations in three intervals of particle size.

sizes have a pressure-dependent correction that is independent of the particle size. In Fig. 18, the horizontal dashed lines where $D < 40\,\mu$m represent this constancy. A good approximation to their value is given by $(1000/P)^{0.10}$ and is best at the lowest pressures where small particles may predominate. The curves given as above are plotted so as to be truncated at this amount. At the upper range of sizes, the curves are truncated where the change in the pressure correction becomes almost negligible. A good approximation is $(1000/P)^{0.45}$.

A question remains regarding how to differentiate convective from stratiform situations and thus which formulations are used to represent the ice cloud properties. General circulation models either prognose or

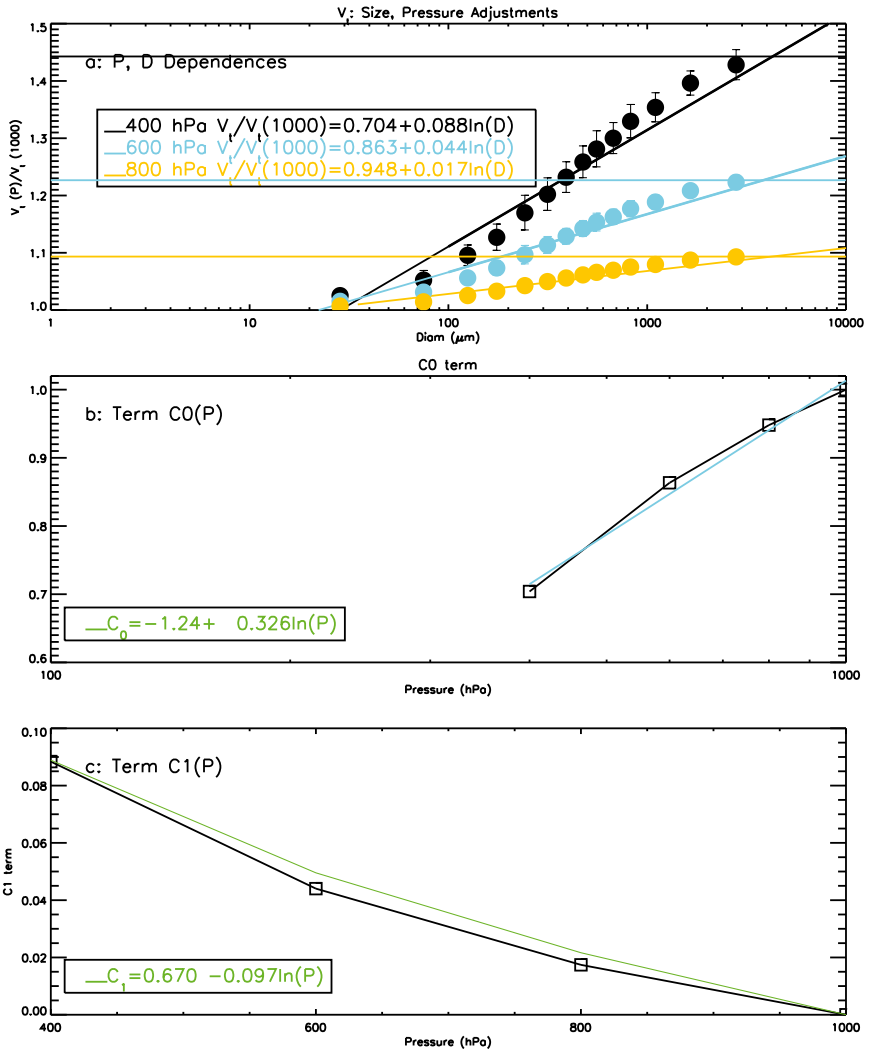

FIG. 17. Adjustments for ice particle terminal velocities as a function of pressure. (a) Correction for V_t as a function of particle diameter for three pressure levels, with a logarithmic fit to the results of the form $C = C_0 + C_1 \ln(D)$. Horizontal lines show the correction amount for the indicated pressures by assuming solely a $(1000/P)^{0.4}$ dependence. (b) Term C_0 as a function of pressure and a fit to the data. (c) As in (b), but for term C_1.

diagnose the IWC, and the IWC is also retrieved from *CALIPSO* and *CloudSat* observations. Figure 19 shows the distributions of the IWC derived from the gamma fits (measured values are noisier because of hysteresis and other factors) as a function of temperature, partitioned by convective and stratiform situations. There is obviously considerable scatter in the data, but in the mean the IWCs are higher in the convective situations than in the stratiform cases. In the former, water-saturated conditions are expected for much of the ice particle growth period, whereas in the latter conditions are closer to ice saturation (Korolev and Isaac 2006). To a first approximation, the temperature dependence of $\Delta\rho$, the difference between the saturation vapor densities over water [using the Goff–Gratch (Goff and Gratch 1946) formulation] and ice (Hyland and Wexler 1983), appears to represent the IWC in the convectively generated ice cloud and 25% of these values the IWC in stratiform cloud. These relationships hold for temperatures below −20°C but not surprisingly lie above the peak in the $\Delta\rho$ curve at −12°C (Fig. 19). Curve fits to the actual data are quite close to these values (Fig. 19).

4. Summary and conclusions

Microphysical properties of ice cloud layers formed directly or indirectly by deep convection and large-scale lifting are investigated using in situ observations from 10

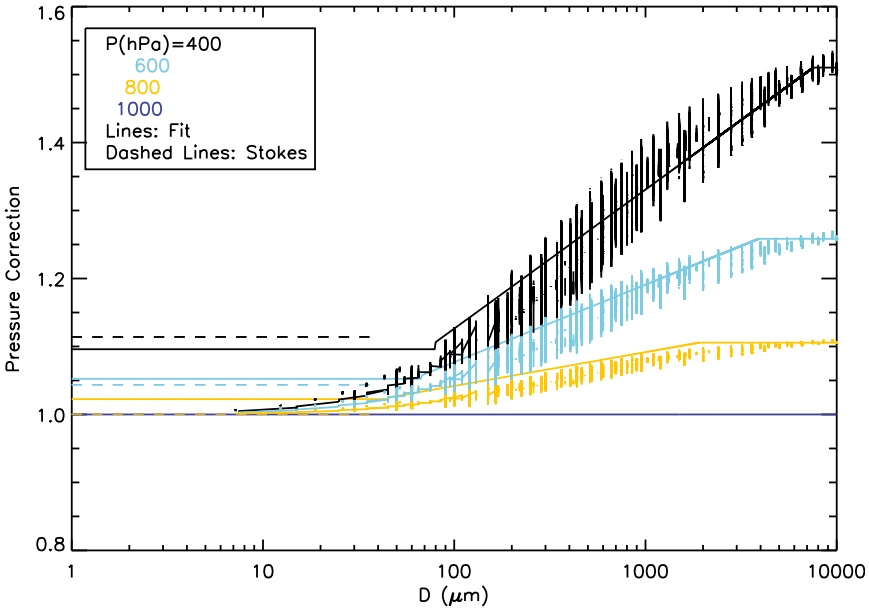

FIG. 18. Pressure correction for all data points at each of three pressure levels (vertical lines are comprised of large numbers of data points) and the results of the fits given in Fig. 17. The dashed horizontal lines show the pressure correction for Stokes-size ice spheres.

field programs. The data were collected at latitudes ranging from 12°S to 70°N, longitudes from 148°W to 130°E, altitudes from near the surface to 18.7 km, and with temperatures from 0° to −86°C. The composite dataset includes more than 85 000 in-cloud size distributions, each spanning horizontal pathlengths of 750–1000 m, or a total of about 800 000 km. Balloonborne ascents through ice cloud layers are included in the

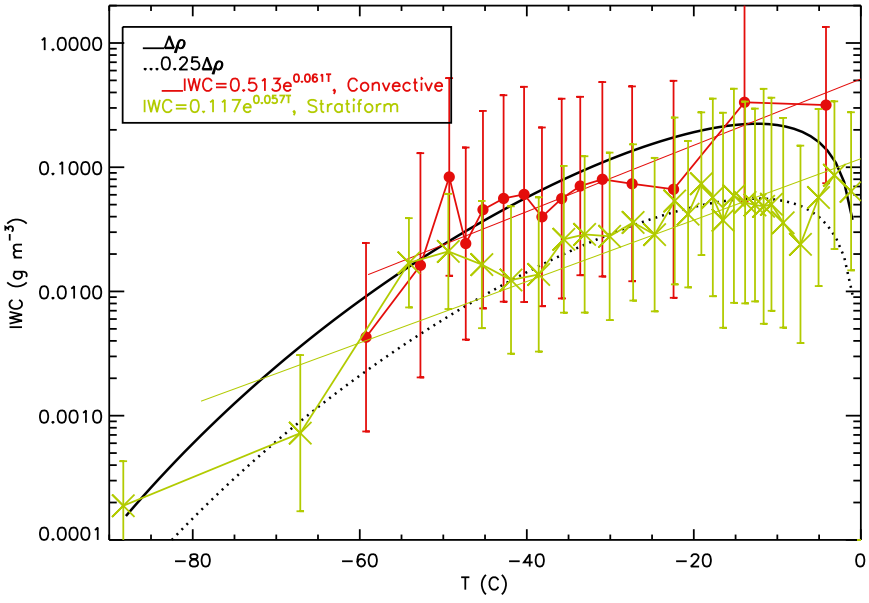

FIG. 19. Relationship between the IWC as a function of temperature for the convective and stratiform clouds. Median values are shown in intervals of an equal number of points. The solid lines are curve fits to the median values for temperatures −25°C and above. The Hyland and Wexler (1983) formulation is used to derive the saturation vapor density of water vapor and the Goff–Gratch equation (Goff and Gratch 1946) for that of ice. The dotted lines show the difference between these two amounts as a function of temperature.

TABLE 3. Summary of equations fitted to the data.

IWC scaling factor (Fig. 3b)	Cold temperatures: $\mathrm{IWC} = \begin{cases} \mathrm{IWC_{PSD}} \times 0.69(\mathrm{IWC_{PSD}})^{-0.051}, & \mathrm{IWC} < 0.0006\ \mathrm{g\,m^{-3}} \\ \mathrm{IWC_{PSD}}, & \mathrm{IWC} \geq 0.0006\ \mathrm{g\,m^{-3}} \end{cases}$
	Warm temperatures: $\mathrm{IWC} = \begin{cases} \mathrm{IWC_{PSD}} \times 1.83(\mathrm{IWC_{PSD}})^{0.192}, & \mathrm{IWC} \geq 0.04\ \mathrm{g\,m^{-3}} \\ \mathrm{IWC_{PSD}}, & \mathrm{IWC} < 0.04\ \mathrm{g\,m^{-3}} \end{cases}$
Total ice concentration (Fig. 4)	$N_t \approx 27\mathrm{L}^{-1}$, $T \leq -60°\mathrm{C}$
	$N_t = 3.304e^{-0.046\,07T}$, $T > -60°\mathrm{C}$
Temperature dependence of PSD maximum diameter (Fig. 6)	$D_{\max} = \begin{cases} 2.6e^{0.0804T}, & T < -36°\mathrm{C}, & \text{composite} \\ 1.0e^{0.0547T}, & T \geq -36°\mathrm{C}, & \text{composite} \\ 1.1e^{0.069T}, & & \text{stratiform} \\ 2.1e^{0.070T}, & & \text{convective} \end{cases}$
Maximum diameter relationship with PSD slope (Fig. 7a)	$D_{\max} = \begin{cases} 0.71\lambda^{-0.64}, & T \leq -60°\mathrm{C} \\ 4.36\lambda^{-0.77}, & T > -60°\mathrm{C} \end{cases}$
Maximum diameter relationship with temperature (Fig. 7b)	$\lambda = \begin{cases} 9.88e^{-0.060T}, & T < -58°\mathrm{C}, & \text{composite} \\ 0.75e^{-0.1057T}, & T \geq -58°\mathrm{C}, & \text{composite} \\ 15.3e^{-0.053T}, & & \text{stratiform} \\ 3.4e^{-0.083T}, & & \text{convective} \end{cases}$
PSD dispersion as a function of PSD slope (Fig. 9a)	$\mu = \begin{cases} 1.5\lambda^{0.223} - 3, & \lambda > -0.56, & \text{stratiform} \\ 0.6\lambda^{0.382} - 3, & \lambda > -1.46, & \text{convective} \\ 0.9\lambda^{0.308} - 3, & \lambda > -0.94, & \text{all data} \end{cases}$
PSD dispersion as a function of temperature (Fig. 9b)	$\mu = \begin{cases} -0.001\,58 - 0.031T, & & & \text{stratiform} \\ -1.68 - 0.051T, & & & \text{convective} \\ -14.09 - 0.248T, & & T < -61°\mathrm{C}, & \text{composite} \\ -0.59 - 0.030T, & & T \geq -61°\mathrm{C}, & \text{composite} \\ -0.84 - 0.0915T - 2.93 \times 10^{-3}T^2 - 3.653 \times 10^{-5}T^3 - 2.157 \times 10^{-8}T^4, & & \text{all temperatures} & \text{composite} \end{cases}$
Area ratio parameter alpha vs temperature (Fig. 11a)	$\alpha = \begin{cases} 0.25e^{0.0161T}, & T > -60°\mathrm{C}, & \text{composite} \\ 0.2833 + 6.913 \times 10^{-3}T + 8.09 \times 10^{-5}T^2, & \text{all temperatures} & \text{composite} \end{cases}$
Area ratio parameter beta vs temp. (Fig. 11b)	$\beta = \begin{cases} -0.25 + 0.0033T, & T > -60°\mathrm{C} \\ -0.2026 + 9.681 \times 10^{-3}T + 1.19 \times 10^{-4}T^2, & \text{all temperatures} \end{cases}$ composite
Area ratio parameter alpha vs beta (Fig. 11c)	$\beta = 2.14 + 0.261\,01[\ln(\alpha)]$, composite (all)
Fractal dimension coefficient b as a function of temperature (Fig. 12a)	$b = 2.31 + 0.0054T$, composite (all)
Fractal dimension coefficient as a function of temperature (Fig. 12b)	$a = 0.0081e^{0.013T}$

TABLE 3. (*Continued*)

Terminal velocity as a function of particle diameter	$V_t(\text{cm s}^{-1}) = 0.0028D^{2.00}$	$D < 41\ \mu$m,	stratiform
	$0.0791D^{1.101}$	$41 < D < 839\ \mu$m,	stratiform
	$62.29D^{0.1098}$	$D > 839\ \mu$m,	stratiform
	$0.0028D^{2.00}$	$D < 56\ \mu$m,	convective
	$0.1194D^{1.0697}$	$56 < D < 640\ \mu$m,	convective
	$21.90D^{0.2629}$	$D > 640\ \mu m$,	convective
	$\sum_{i=0}^{4} q_i D^{r_i}$, where $q_{(i=0\text{to}4)} = -1.5791, 0.175\,16, -5.597\,92 \times 10^{-5}, 3.221\,07 \times 10^{-9}, 0,$	$D > 11\ \mu$m	stratiform
	where $q_{(i=0\text{to}4)} = -2.9643, 0.2282, -0.000\,111\,007, 2.181\,18 \times 10^{-8}, -1.131\,15 \times 10^{12},$	$D > \ \mu$m	convective
Pressure dependence of terminal velocities f(diameter) (Fig. 17a)	$V_t(P)/V_t(1000) = 0.704 + 0.088[\ln(D)]$,	$P = 400$ hPa	
	$0.863 + 0.044[\ln(D)]$,	$P = 600$ hPa	
	$0.948 + 0.017[\ln(D)]$,	$P = 800$ hPa	
Term c_0 in pressure-dependent correction to terminal velocity (Fig. 17b)	$c_0 = -1.24 + 0.326[\ln(P)]$		
Term c_1 in pressure-dependent correction to terminal velocity (Fig. 17c)	$c_1 = 0.670 - 0.097[\ln(P)]$		
Mass-weighted diameter	$D_m = (b + \mu + 0.67)/\lambda$, where $b \sim 2.05$ is the exponent in the $m(D)$ relationship		
Mass-weighted fall speed	Calculated from V_t, relationship using D_m for D and associated pressure P		
IWC distribution with temperature (Fig. 19)]	$\text{IWC} = 0.117e^{0.057T}$,	stratiform	
	$0.513e^{0.061T}$,	convective	

dataset. This dataset is representative of the wide range of conditions where ice clouds are found in the troposphere and lower stratosphere on a near-global scale. A full set of equations developed to represent the observations and representations is presented in Table 3.

Direct measurements of the total condensate water content were measured in 9 of the 10 field programs. Mixed-phase regions have been excluded. Particle size distributions beginning at 2–10 μm for the samples with temperatures below −60°C and larger than about 50 μm for the warmer clouds extending to several centimeters were measured. We suggest that the PSDs measured at temperatures above −60°C include most of the ice crystals present, assuming that water saturation or nearly water saturation exists during the nucleation and early growth of the ice crystals at temperatures above −35° or −40°C where heterogeneous ice nucleation dominates. Based on the ice growth rate calculations of Westbrook and Heymsfield (2011; calculations by C. Westbrook), the times required to grow 100-μm pristine plate and columnlike ice crystals are only 100 s or less where the temperatures are warmer than −40°C, increasing to several hundred seconds as temperatures decrease to −60°C. These calculations assume a standard atmosphere, pressure levels corresponding approximately to the measurements, and water saturation conditions, which, unless secondary ice production processes occur in a temperature range outside of the Hallett–Mossop zone or breakup occurs, is likely to be present during the early growth phase.

The total ice concentrations N_t generally fall in the range 5–100 L^{-1}, with a gradual decrease noted with increasing temperature in the mean values: 25–50 L^{-1} at −60°C and below to about 5 L^{-1} near 0°C. This decreasing trend could be the result of aggregation and ice nucleation processes. A small enhancement in N_t observed around −5°C is likely due to secondary ice production process associated with the needles that we observed close to this temperature. Although the growth rates of small needles are very high and they should grow rapidly to our detection size, this local enhancement may be even larger.

Of note is that on average the size distributions broaden with temperature, with larger and more numerous particles observed in the clouds that we associate with convection. The largest particle size in the measured PSDs increases from about 50 μm to above 1 cm over the −86° to 0°C temperature range, reflecting the increase in water vapor available and aggregation for growth and fewer particles at the warmer temperatures.

The particle size distributions are fitted to gamma functions. The PSD slope decreases by three orders of magnitude over the observed temperature range, much like the observations at warmer temperatures from earlier studies. The PSD dispersion crosses from values just above 0 to just below for temperatures between about −40° and −15°C, indicating approximate exponentiality in this range. The exponentiality in this range is likely due to aggregation—more larger aggregates at the expense of the smaller particles. Below −40°C, the concentrations of small particles diverge above an exponential while above −15°C, small particle concentrations diverge below exponential. A fractal analysis suggests that the exponent in the mass–dimensional relationship of 2.1 (trending from about 2.0 to 2.3 from −60° to 0°C) is reasonable for use across all temperatures, rather than the commonly assumed value of 1.9 or a constant density with size. The PSDs, together with an average mass–dimensional relationship that is consistent with the mean value derived from the fractal analysis, provide a good estimate of the IWC across the range 0.01–1 g m^{-3}. For lower temperatures, the relationship developed by Schmitt and Heymsfield (2009) fits the measured values for temperatures below −60°C.

Area–dimensional relationships suggest that particles become more ''filled in'' between −40° and 0°C, again suggestive of increasing aggregation downward in the cloud layers. As temperatures decrease below −40°C, the area–dimensional analyses indicate that the particles are less filled in, suggesting pristine, more single, platelike crystals.

New and more accurate estimates of ice fall speeds that cover the sizes where most of the IWC is contained have been derived, including improved corrections for pressure. It is demonstrated that pressure corrections in earlier studies are producing estimates of V_t that are much too large for the smaller particles found in the upper troposphere. This overestimate could lead to ice cloud lifetimes in GCMs that are unrealistically short leading to cloud radiative properties that are biased low. This error needs to be addressed in climate models with prescribed fall speeds.

Relationships expressing particle size distributions, area–dimensional analyses, and fall speeds are presented in terms of their generation associated with convective and stratiform clouds, with the distribution of IWC with temperature showing strong differences. The relationships developed can serve as a basis for developing reliable parameterizations for deducing ice cloud microphysical properties from *CALIPSO* lidar extinction, *CloudSat* radar reflectivities, and forthcoming spaceborne Doppler cloud radar. Improvements of ice cloud particle properties in GCMs using our new results are warranted.

Acknowledgments. The authors wish to thank the funding provided by the *CALIPSO* and *CloudSat* project

offices, Dave Winker and Deb Vane, respectively, NASA GPM Contract NNX10AH67G (Ramesh Kakar, project manager), the NSF Science and Technology Center for Multiscale Modeling at CSU CMMAP, and DOE/ARM (Grant DE-FG02-08ER64575). We wish to thank Chris Westbrook for calculating growth times to 100 microns and Cornelius Schiller and Susan Rohr for providing the SCOUT data. Meg Miller's editorial assistance is greatly appreciated.

APPENDIX A

Lower Size Limit of Particle Size Distributions

This appendix examines the question of whether the 2DC and CIP probes adequately measure the PSDs to a size below a few hundred microns and whether the FSSP or CAS reliably add PSD information below 50 μm for temperatures above about −60°C.

If shattering on the inlets of the small particle probes is ignored, derived properties of the PSDs would be unreliable where shattering is appreciable—largely for the observations above −60°C. As an example, factoring in the FSSP data to the imaging-probe PSDs from CF would increase the IWC by a median value of 14% and total particle cross-sectional area by 46%. To identify and quantify the signature of shattering, the data from the small particle probes was examined in different ways.

The effective diameter, given by $D_e = 3.29(\text{IWC}/\sigma)$ (Mitchell 2002), provides a good identification parameter and approximately represents a mean particle size. As temperature and the corresponding IWC decrease, the addition of FSSP data should yield an increasing deviation of D_e from the 2D probe data alone. This trend is shown by the connected line in Fig. A1, where D_e for one ascent through cloud from the replicator dataset, our most reliable small particle dataset, is plotted. At cloud top, where D_e should be small, the inclusion of the small (<50 μm) particles (ordinate) produces much lower values than with the large particles alone (abscissa). The ensemble of particles grows downward and then sublimate toward the base of the cloud, yielding a ''true'' pattern. By comparison, the inclusion of FSSP data from several field programs produces a nearly linear offset of D_e, suggesting that the small particles are primarily produced by shattering of the larger, 2D particles. Deviations from this linearity may be the result of real, small particles—especially from MPACE, but the signature appears to be dominated by shattering of larger particles.

Are we measuring most of the total concentration with the size detection thresholds chosen? To examine this point, we draw upon the growth rate calculations in Westbrook and Heymsfield (2011) and aspect ratio (length/width) data from laboratory studies. We use a standard atmosphere to prescribe temperatures and pressure for temperatures between −60° and 0°C and assume ambient vapor densities at water saturation as a first approximation. The times required to grow plates from 1 to 100 μm—where the concentrations from the 2D probes are likely to be accurate—range from 10 s at temperatures near −10°C to as much as 400 s at −60°C; for columns, the corresponding times are several seconds to 80 s. Given the 2-μm (SCOUT) to 10-μm (Replicator, VIPS) detection size for the <−60°C observations and 50 μm for the >−60°C observations, N_t values derived from the respective particle probes probably include most ice crystals present in each temperature range.

We further investigate our assumption of omitting the small particles using TC4 data. CAS PSDs and those from the CIP and PIP (hereafter PP) from the 8 August flight are examined. The ice cloud sampled was formed through deep convection that extended to a height of 13 km as ascertained from radar and lidar data from the ER-2 aircraft that overflew the DC8. Multiple, constant-altitude penetrations included six constant-altitude passes from just below cloud top to about 4 km into the cloud at temperatures T from −57° to −34°C. The flight from this day was used because it was one of the few days from TC4 when the CAS probe worked well.

To serve as a basis for evaluation of the data from these probes, PSDs measured by the SPEC 2DS probe, with a lower minimum detectable size than the CIP—about 20 μm, and with an improved resolution of 10 rather than 25 μm per size bin—were used. SPEC processed the data. Unfortunately, the 2DS probe did not operate for the lowest-temperature penetration at −57°C, but coincident data were obtained by all probes for the other penetrations.

Concentrations are examined over different size ranges for the evaluation: (i) all 2DS PSDs above 10 μm and CIP+PIP PSDs above 50 μm; (ii) 2DS PSDs above 20 μm and CIP+PIP PSDs above 50 μm; (iii) 2DS PSDs above 40 μm and CIP+PIP PSDs above 50 μm, where there are overlapping sizes between the probes; (iv) 2DS PSDs above 100 μm and CIP+PIP PSDs above 100 μm, again in an overlapping size range; and (v) the ratio of the CAS to CIP concentrations and indirectly to the 2DS concentrations.

In Figs. A2a and A2b, we note that the 2DS concentration for (i) is more than a factor of 2 larger than that from the PP. This disagreement is vastly reduced for (ii). In overlapping size ranges (iii, iv), the PP concentrations are 10% larger than those of the 2DS. The CAS concentrations in (v) are higher than those from the PP by

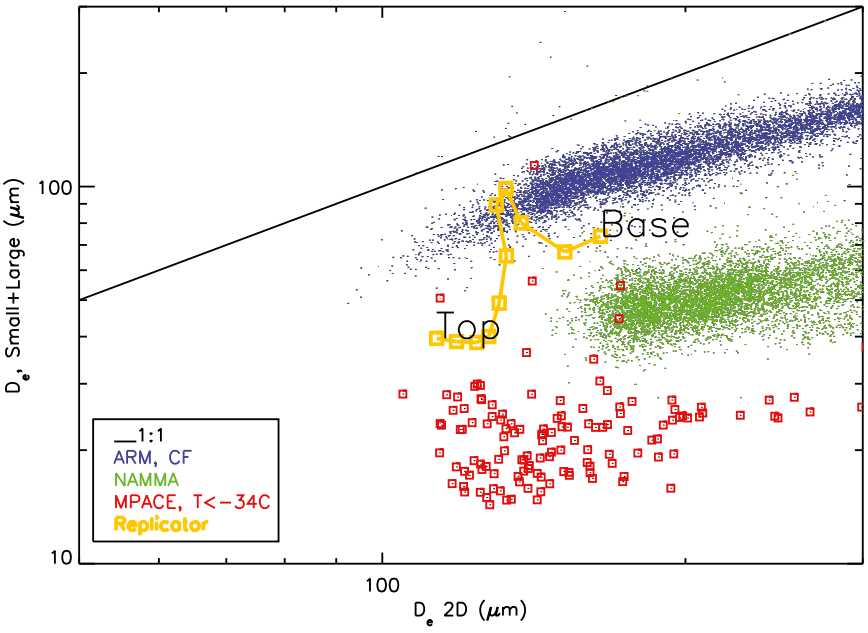

FIG. A1. Effective diameter derived from the 2D imaging-probe data relative to the combination from the 2D and small-particle probes. The colored curve shows the values derived from a balloonborne ascent through a cirrus cloud at temperatures from −52° to −40°C. The points shown are smoothed using a three-position smoothing. Data from ARM and CF are combined because the particle probes and aircraft were the same.

a factor of 400 and higher than those from the 2DS probe by a factor of 200. It is noted that for (v), the ratio of the CAS to PP concentrations is nearly constant for all penetration temperatures; thus, it is likely that the CAS accepts a certain fraction of the shattered large particles.

The coincident concentrations cover the temperature range from −53° to −12°C (Fig. A2b). For (ii), we note some elevated concentrations for T below −48°C relative to the PP. These may be real particles that were sampled near cloud top. Otherwise, for (ii) the ratio of 2DS to PP concentrations are nearly constant with temperature. For (i), we note that the ratio of 2DS to PP concentration is elevated across the sampling temperature range. Because there were no special tips on the front end of the 2DS probe for TC4, we suggest the possibility that occasional small particles produced by shattering that entered the field of view of the probe could not be identified from particle interarrival times (Field et al. 2006), thus leading to a significantly overestimated concentration because of the depth of field–sampling volume relationship.

Our best assessment of the performance of the CAS and PP probes for temperatures above −60°C can be drawn from Fig. A2 and a summary given in the text box of Fig. A2b. The CAS concentration is dominated by artifacts and does not provide useful information. The concentrations for the PP for sizes 50 μm and above are nearly the same as for the 2DS concentration above 20 μm. Increasing the PP cutoff size to 100 μm appreciably reduces the concentration relative to the 50-μm cutoff size.

While the agreement between PP and 2DS is strong when including particles smaller than 100 μm, there is still considerable uncertainty in the optical depth of field for particles of this size. Furthermore, the measurement of particles that shadow only a few pixels is inherently uncertain, and differentiation between natural particles and artifacts of this size can be very difficult. The agreement between PP and 2DS was even more robust when using particles larger than 100 μm, and we therefore recommend and use this approach when reporting total particle number concentrations from optical array probes.

APPENDIX B

SCOUT FSSP Sizing

The IWCs derived from the SCOUT 5-s-average PSDs were systematically and uniformly lower than measured by the FISH–FLASH combination (Fig. B1a). Because the FSSP PSDs for SCOUT dominate the IWC across the entire range of IWCs for the temperatures considered here (and solely for SCOUT), Fig. B1a suggests that the FSSP sizing is biased low. Figure B1b derives the

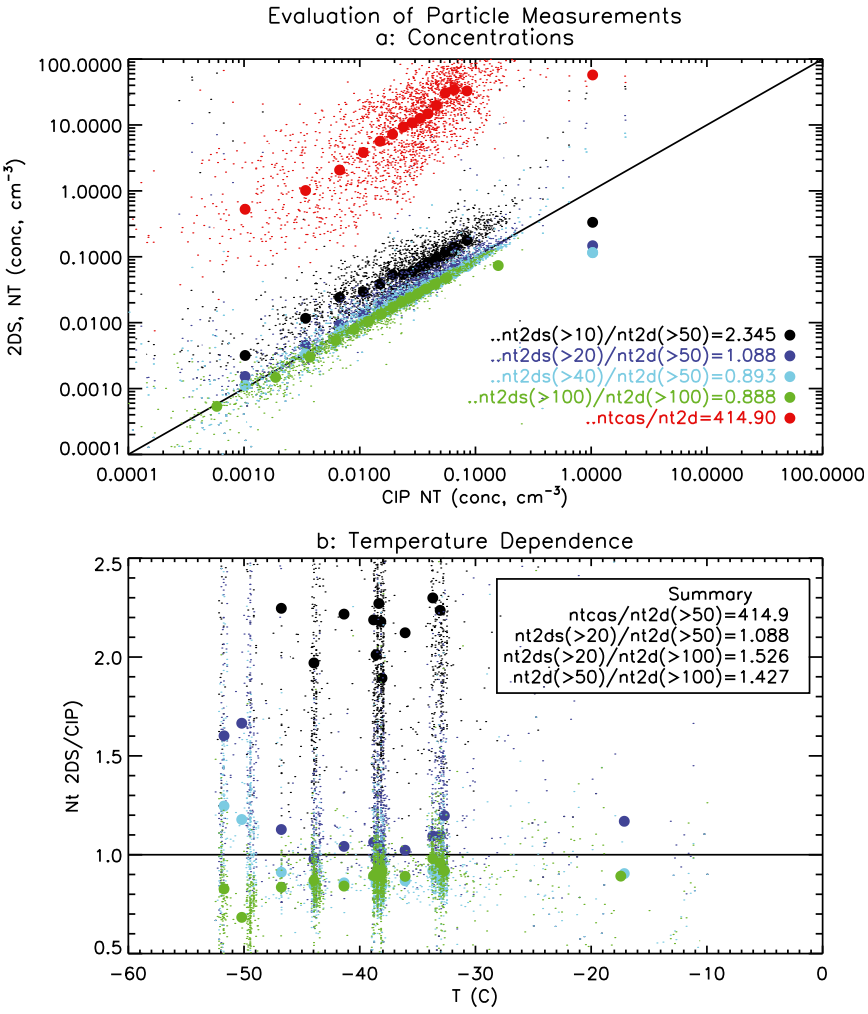

FIG. A2. Comparison of concentrations measured by the CIP and PIP particle probes (PP) and those from the CAS and 2DS probes for the 8 Aug TC4 case study. (a) Comparison of concentrations. (b) As in (a), but the ordinate is the ratio of concentrations with various assumptions vs temperature. The CAS ratios are not shown in (b), because it would reduce the legibility of the goals of the figure.

IWC by assuming that all FSSP particles are undersized by a factor of 1.80—the amount that gives a good match with the FISH instrument. This comparison suggests that an equivalent spherical diameter of 1.80 times the nominal FSSP sizing reliably reproduces the measured IWC. Cotton et al. (2010) conduct a detailed analysis of the undersizing of ice particles by the FSSP using the small ice detector probe, yielding a factor of 1.7 needed to correct the data, and Baumgardner et al. (2012) note that ''Because the optical scattering cross section is sensitive to the orientation of the particle, as well as to the degree of asphericity, a large degree of undersizing, sometimes more than a factor of 2, cannot be avoided when size distributions are reported from instruments like the FSSP.'' Note, however, that our choice of a 1.80 factor is only a comparison and it may not be realistic because all sizes are corrected uniformly and the FSSP is known to broaden the PSDs.

Lognormal and gamma fits to size-adjusted PSDs give continuous PSDs, somewhat counteracting the sample-volume limitation of the FSSP. The gamma form, when integrated over the range from the minimum considered to probe maximum measured size, slightly underestimates the measured IWC (Fig. 3c) but lowers the standard deviation; by extending the fitted PSD to twice the measured diameter to account for sample-volume limitations of the probes, it produced IWCs slightly above those from the observations (Fig. 3d). Further increasing the extrapolated diameter used to calculate the IWC from the gamma PSDs did little to change the

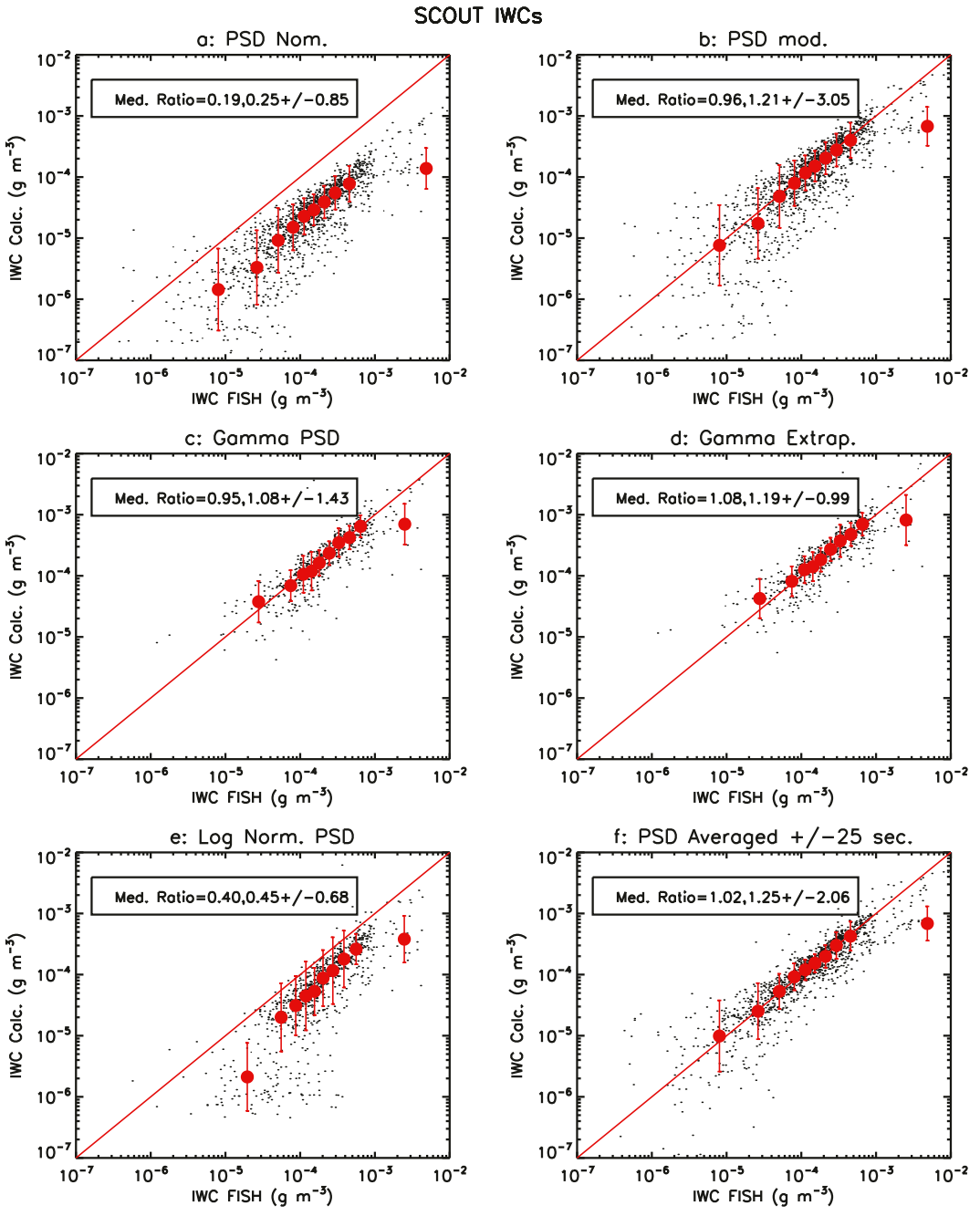

FIG. B1. Ice water content calculated from the SCOUT PSDs compared to IWCs measured by the FISH probe. (a) The calculated IWCs using the nominal probe bin sizes compared to the measured IWCs. (b) As in (a), but with bin sizes adjusted as noted in the text. (c)–(e) IWCs derived from fitted functions. (f) As in (b), but with IWCs derived by averaging of the PSDs either side of the measured PSDs. Median values of the ratio of the calculated to measured IWC for all data combined and the standard deviation for all IWC values are listed in each panel.

results. The IWCs derived from the lognormal PSDs substantially underestimated the measured IWC (Fig. 3e).

The IWCs were also calculated from the PSDs smoothed using a boxcar average between the measured PSD and the PSDs ±10 s on either side of it to increase the number of particles sampled (Fig. 3f). The excellent match of this IWC to the measured values points to the need to average over more than 5-s periods (especially important given the small sample volume of the FSSP) or to use the extrapolated gamma fits, which account for

the relatively small sample size of the particles at the large end of each measured PSD.

REFERENCES

Baumgardner, D., and Coauthors, 2012: In situ, airborne instrumentation: Addressing and solving measurement problems in ice clouds. *Bull. Amer. Meteor. Soc.,* **93,** ES29–ES34.

Brown, P. R. A., and P. N. Francis, 1995: Improved measurements of the ice water content in cirrus using a total-water probe. *J. Atmos. Oceanic Technol.,* **12,** 410–414.

Cotton, R. S., T. S. Osborne, Z. Ulanowski, E. Hirst, P. H. Kaye, and R. S. Greenaway, 2010: The ability of the Small Ice Detector (SID-2) to characterize cloud particle and aerosol morphologies obtained during flights of the FAAM BAe-146 research aircraft. *J. Atmos. Oceanic Technol.,* **27,** 290–303.

Davis, S. M., L. M. Avallone, E. M. Weinstock, C. H. Twohy, J. B. Smith, and G. L. Kok, 2007: Comparisons of in situ measurements of cirrus cloud ice water content. *J. Geophys. Res.,* **112,** D10212, doi:10.1029/2006JD008214.

Delanoë, J., A. Protat, J. Testud, D. Bouniol, A. J. Heymsfield, A. Bansemer, P. R. A. Brown, and R. M. Forbes, 2005: Statistical properties of the normalized ice particle size distribution. *J. Geophys. Res.,* **110,** D10201, doi:10.1029/2004JD005405.

Demott, P. J., and Coauthors, 2010: Predicting global atmospheric ice nuclei distributions and their impacts on climate. *Proc. Natl. Acad. Sci. USA,* **107,** 11 217–11 222.

de Reus, M. S., and Coauthors, 2009: Evidence for ice particles in the tropical stratosphere from in situ measurements. *Atmos. Chem. Phys.,* **9,** 6775–6792.

Falconer, K., 2003: *Fractal Geometry Mathematical Foundations and Applications.* Wiley, 337 pp.

Field, P. R., R. J. Hogan, P. R. A. Brown, A. J. Illingworth, T. W. Choularton, and R. J. Cotton, 2005: Parametrization of ice-particle size distributions for mid-latitude stratiform cloud. *Quart. J. Roy. Meteor. Soc.,* **131,** 1997–2017.

——, A. J. Heymsfield, and A. Bansemer, 2006: Shattering and particle interarrival times measured by optical array probes in ice clouds. *J. Atmos. Oceanic Technol.,* **23,** 1357–1371.

——, ——, and ——, 2007: Snow size distribution parameterization for midlatitude and tropical ice clouds. *J. Atmos. Sci.,* **64,** 4346–4365.

Gardiner, B. A., and J. Hallett, 1985: Degradation of in-cloud forward scattering spectrometer probe measurements in the presence of ice particles. *J. Atmos. Oceanic. Technol.,* **2,** 171–180.

Goff, J. A., and S. Gratch, 1946: Low-pressure properties of water from −160° to 212°F. *Transactions of the American Society of Heating and Ventilating Engineers,* Vol. 26, American Society of Heating and Ventilating Engineers, 95–122.

Hartmann, D. L., and D. A. Short, 1980: On the use of earth radiation budget statistics for studies of clouds and climate. *J. Atmos. Sci.,* **37,** 1233–1250.

Heymsfield, A. J., 2003: Properties of tropical and midlatitude ice cloud particle ensembles. Part II: Applications for mesoscale and climate models. *J. Atmos. Sci.,* **60,** 2573–2591.

——, and C. M. R. Platt, 1984: A parameterization of the particle size spectrum of ice clouds in terms of the ambient temperature and the ice water content. *J. Atmos. Sci.,* **41,** 846–855.

——, and L. M. Miloshevich, 2003: Parameterizations for the cross-sectional area and extinction of cirrus and stratiform ice cloud particles. *J. Atmos. Sci.,* **60,** 936–956.

——, and C. D. Westbrook, 2010: Advancements in the estimation of ice particle fall speeds using laboratory and field measurements. *J. Atmos. Sci.,* **67,** 2469–2482.

——, A. Bansemer, P. R. Field, S. L. Durden, J. L. Stith, J. E. Dye, W. Hall, and C. A. Grainger, 2002: Observations and parameterizations of particle size distributions in deep tropical cirrus and stratiform precipitating clouds: Results from in situ observations in TRMM field campaigns. *J. Atmos. Sci.,* **59,** 3457–3491.

——, P. R. Field, and A. Bansemer, 2008: Exponential size distributions for snow. *J. Atmos. Sci.,* **65,** 4017–4031.

——, A. Bansemer, G. Heymsfield, and A. O. Fierro, 2009: Microphysics of maritime tropical convective updrafts at temperatures from −20° to −60°C. *J. Atmos. Sci.,* **66,** 3530–3562.

——, C. Schmitt, A. Bansemer, and C. H. Twohy, 2010: Improved representation of ice particle masses based on observations in natural clouds. *J. Atmos. Sci.,* **67,** 3303–3318.

Houze, R. A., P. V. Hobbs, P. H. Herzegh, and D. B. Parsons, 1979: Size distributions of precipitation particles in frontal clouds. *J. Atmos. Sci.,* **36,** 156–162.

Hyland, R. W., and A. Wexler, 1983: Formulations for the thermodynamic properties of the saturated phases of H_2O from 173.15 K to 473.15 K. *ASHRAE Trans.,* **89** (2A), 500–519.

Ikawa, M., and K. Saito, 1991: Description of a non-hydrostatic model developed at the Forecast Research Department of the MRI. MRI Tech. Rep. 28, 238 pp.

Isaac, G. A., S. G. Cober, J. W. Strapp, D. Hudak, T. P. Ratvasky, D. L. Marcotte, and F. Fabry, 2005: Preliminary results from the Alliance Icing Research Study (AIRS). *Proc. AIAA 43rd Aerospace Sciences Meeting and Exhibit,* Reno, NV, AIAA, 2005-252. [Available online at http://airs-icing.org/publications/Isaac%20-%20AIAA2001.pdf.]

Jameson, A. R., and A. J. Heymsfield, 2013: A Bayesian approach to upscaling and downscaling of aircraft measurements of ice particle counts and size distributions. *J. Appl. Meteor. Climatol.,* **52,** 2075–2088.

Jensen, E. J., and Coauthors, 2009: On the importance of small ice crystals in tropical anvil cirrus. *Atmos. Chem. Phys.,* **9,** 5519–5537.

King, W. D., 1986: Air flow and particle trajectories around aircraft fuselages. IV: Orientation of ice crystals. *J. Atmos. Oceanic Technol.,* **3,** 433–439.

Korolev, A. V., and G. A. Isaac, 2005: Shattering during sampling by OAPs and HVPS. Part I: Snow particles. *J. Atmos. Oceanic Technol.,* **22,** 528–542.

——, and ——, 2006: Relative humidity in liquid, mixed-phase, and ice clouds. *J. Atmos. Sci.,* **63,** 2865–2880.

——, E. F. Emery, J. W. Strapp, S. G. Cober, G. A. Isaac, M. Wasey, and D. Marcotte, 2011: Small ice particles in tropospheric clouds: Fact or artifact? Airborne Icing Instrumentation Evaluation Experiment. *Bull. Amer. Meteor. Soc.,* **92,** 967–973.

Lawson, R. P., D. O'Connor, P. Zmarzly, K. Weaver, B. Baker, Q. Mo, and H. Jonsson, 2006: The 2DS (stereo) probe: Design and preliminary tests of a new airborne, high-speed, high-resolution, particle imaging probe. *J. Atmos. Oceanic Technol.,* **23,** 1462–1477.

Li, J.-L., and Coauthors, 2005: Comparisons of EOS MLS cloud ice measurements with ECMWF analyses and GCM simulations: Initial results. *Geophys. Res. Lett.,* **32,** L18710, doi:10.1029/2005GL023788.

——, J. H. Jiang, D. E. Waliser, and A. M. Tompkins, 2007: Assessing consistency between EOS MLS and ECMWF analyzed

and forecast estimates of cloud ice. *Geophys. Res. Lett.,* **34,** L08701, doi:10.1029/2006GL029022.

Lin, Y.-L., R. D. Farley, and H. D. Orville, 1983: Bulk parameterization of the snow field in a cloud model. *J. Climate Appl. Meteor.,* **22,** 1065–1092.

Locatelli, J. D., and P. V. Hobbs, 1974: Fall speeds and masses of solid precipitation particles. *J. Geophys. Res.,* **79,** 2185–2197.

McFarquhar, G. M., and A. J. Heymsfield, 1997: Parameterization of tropical ice crystal size distributions and implications for radiative transfer: Results from CEPEX. *J. Atmos. Sci.,* **54,** 2187–2200.

Miloshevich, L. M., and A. J. Heymsfield, 1997: A balloon-borne continuous cloud particle replicator for measuring vertical profiles of cloud microphysical properties: Instrument design, performance, and collection efficiency analysis. *J. Atmos. Oceanic Technol.,* **14,** 753–768.

Mitchell, D. L., 1996: Use of mass- and area-dimensional power laws for determining precipitation particle terminal velocities. *J. Atmos. Sci.,* **53,** 1710–1723.

——, 2002: Effective diameter in radiation transfer: General definition, applications, and limitations. *J. Atmos. Sci.,* **59,** 2330–2346.

Rutledge, S. A., and P. V. Hobbs, 1984: The mesoscale and microscale structure and organization of clouds and precipitation in midlatitude cyclones. XII: A diagnostic modeling study of precipitation development in narrow cold-frontal rainbands. *J. Atmos. Sci.,* **41,** 2949–2972.

Sanderson, B. M., C. Piani, W. J. Ingram, D. A. Stone, and M. R. Allen, 2008: Towards constraining climate sensitivity by linear analysis of feedback patterns in thousands of perturbed-physics GCM simulations. *Climate Dyn.,* **30,** 175–190.

Schiller, C., M. Kramer, A. Afchine, N. Spelten, and N. Sitnikov, 2008: Ice water content of Arctic, midlatitude and tropical cirrus. *J. Geophys. Res.,* **113,** D24208, doi:10.1029/2008JD010342.

Schmitt, C. G., and A. J. Heymsfield, 2009: The size distribution and mass weighted terminal velocity of low-latitude tropopause cirrus crystal populations. *J. Atmos. Sci.,* **66,** 2013–2028.

——, and ——, 2010: Dimensional characteristics of ice crystal aggregates from fractal geometry. *J. Atmos. Sci.,* **67,** 1605–1616.

Stephens, G. L., and Coauthors, 2002: The CloudSat mission and the A-Train: A new dimension of space-based observations of clouds and precipitation. *Bull. Amer. Meteor. Soc.,* **83,** 1771–1790.

Strapp, J. W., F. Albers, A. Reuter, A. V. Korolev, U. Maixner, E. Rashke, and Z. Vukovic, 2001: Laboratory measurements of the response of a PMS OAP-2DC. *J. Atmos. Oceanic Technol.,* **18,** 1150–1170.

Tian, L., G. M. Heymsfield, L. Li, A. J. Heymsfield, A. Bansemer, C. H. Twohy, and R. C. Srivastava, 2010: A study of cirrus ice particle size distribution using TC4 observations. *J. Atmos. Sci.,* **67,** 195–216.

Toon, O. B., and Coauthors, 2010: Planning, implementation, and first results of the Tropical Composition, Cloud and Climate Coupling Experiment (TC4). *J. Geophys. Res.,* **115,** D00J04, doi:10.1029/2009JD013073.

Vaughan, G., C. Schiller, A. R. MacKenzie, K. Bower, T. Peter, H. Schlager, N. R. P. Harris, and P. T. May, 2008: SCOUTO3/ACTIVE: High-altitude aircraft measurements around deep tropical convection. *Bull. Amer. Meteor. Soc.,* **89,** 647–662.

Westbrook, C. D., and A. J. Heymsfield, 2011: Ice crystals growing from vapor in supercooled clouds between −2.5° and −22°C: Testing current parameterization methods using laboratory data. *J. Atmos. Sci.,* **68,** 2416–2429.

Wylie, D., D. L. Jackson, W. P. Menzel, and J. J. Bates, 2005: Trends in global cloud cover in two decades of HIRS observations. *J. Climate,* **18,** 3021–3031.

Zhang, G., J. Vivekanandan, E. Brandes, R. Meneghini, and T. Kozu, 2003: The shape–slope relation in observed gamma raindrop size distribution: Statistical error or useful information? *J. Atmos. Oceanic Technol.,* **20,** 1106–1119.